Sensitivity analysis of a nonlinear inversion method for 3D electromagnetic imaging in anisotropic media

O Dorn* H Bertete-Aguirre† J G Berryman‡ G C Papanicolaou§

January 21, 2002

Abstract

We present a detailed sensitivity analysis for a nonlinear electromagnetic inversion method which was introduced earlier by the authors. Whereas the earlier work was restricted to the 3D imaging of *isotropic* structures in the earth from cross-borehole electromagnetic data, the analysis presented here is focused on the imaging of *anisotropic* structures which often have to be taken into account in practical situations. The inversion scheme considered can be described as a single step adjoint field scheme. It avoids calculating huge sensitivity matrices (which we call linearized residual operators) during the inversion and uses only the data corresponding to one source position at a time. Doing so, the action of the adjoint linearized residual operator on the corresponding (filtered) residual vector can be calculated very efficiently by just running one forward and one adjoint Maxwell problem on the most recent best guess for the parameters. The outcome of these two runs is combined to find a correction to the latest best guess. The *anisotropic sensitivity functions* have the property that they decompose the linearized residual operator as well as the corresponding adjoint linearized residual operator. Playing this dual role, they provide useful information about how sources and receivers should be arranged in a given experiment, and which structures in the earth can be expected to be resolved in the inversion from a given data set. In the paper, we present numerical examples of 3D anisotropic sensitivity functions for homogeneous as well as for inhomogeneous background parameter distributions, and discuss their dual role in the nonlinear adjoint field inversion scheme.

*Department of Computer Science, University of British Columbia, 201-2366 Main Mall, Vancouver, B.C., V6T1Z4, Canada, E-mail: dorn@cs.ubc.ca

†Lawrence Livermore National Laboratory, PO Box 808, L-206, Livermore, CA 94551-9900, USA, E-mail: hba@llnl.gov

‡Lawrence Livermore National Laboratory, PO Box 808, L-200, Livermore, CA 94551-9900, USA, E-mail: berryman1@llnl.gov

§Department of Mathematics, Stanford University, Stanford, CA 94305, USA, E-mail: papanico@math.stanford.edu

1 Introduction

In a previous paper the authors have presented a new approach to ElectroMagnetic Induction Tomography (EMIT) based on an adjoint imaging method (Dorn *et al* [22]). EMIT uses magnetic fields generated by currents in wire coils as its sources. These source fields may be produced in one borehole with the received signals (also magnetic fields) being measured in other, more distant boreholes or in combination with surface sources and receivers. The goal of this procedure is to image electrical conductivity variations in the earth. The use of the single step adjoint field method for analyzing such data is new and, therefore, several issues remain about its use and meaning that we would like to clarify in the present paper.

One question that is commonly raised about all electrical imaging methods in the diffusive regime (frequencies $f < 1$ MHz) concerns the issue of resolution. Our physical ideas of resolution are normally based on concepts such as that of the *Rayleigh criterion* for resolving power of an aperture in which two point sources of radiation are considered to be resolvable if the maximum of a diffraction pattern of one source coincides with the first minimum of the other (see Jenkins and White [28]). The spatial separation of two objects that can be resolved then clearly depends on the ratio of the wavelength of the radiating sources and the size of the aperture. When we are considering electromagnetic fields in the diffusive regime, it becomes problematic to define a useful resolution criterion. At very low frequencies such as those used in Electrical Resistance/Impedance Tomography (ERT/EIT) there is no wavelength associated with the signals and the resolution must instead be defined in terms of the numbers of source/receiver electrode pairs and the size of the region being imaged (see Ramirez *et al.* [39]). The mathematically analogous problem in hydrology has also been treated (see Vasco *et al* [45]). For EMIT, the situation is closer to that of ERT/EIT than it is to that of wave propagation problems like seismic, ground penetrating radar, or optics. The wavelength does not provide a useful measure of the method's true resolution. A better approach in this situation is to define sensitivity functions (see for example Spies and Habashy [43]).

Sensitivity relations for inverse problems (or, more generally, parameter estimation problems) have been discussed many times in the literature. For example, a well-known reconstruction method in medical imaging is the filtered backprojection method in x-ray tomography [33], which can be interpreted as a backprojection of filtered x-ray data of the human body along sensitivity functions. These sensitivity functions are concentrated on straight lines connecting the source and receiver positions, and the backprojection takes place uniformly over these lines. A generalization of this procedure can be found in optical tomography (OT) [6], where the straight lines are replaced by 'banana-shaped' regions, which are in fact sensitivity functions distributed over the whole imaging domain with space-dependent weights. These weights are highest in some (banana-shaped) regions connecting the source and the receiver positions, but have nonvanishing values also in more remote areas of the imaging domain. For more details see for example Arridge *et al.* [4, 5, 6] or Dorn [23]. It is clear that the limited resolution in optical tomography compared to x-ray tomography is directly related to this broadening of the sensitivity functions, although it is not clear so far how to quantify this relationship between the two concepts.

The situation in low-frequency electromagnetic imaging is in many ways similar to the optical tomography problem. The physical propagation of signals is in both cases basically diffusive, which lets us expect that similar concepts of resolution should be applicable to both situations. The sensitivity functions in low-frequency EM imaging are, as in optical tomography, distributed over the whole imaging domain. In the geophysical application, this would be the whole earth, although by energy arguments it follows that sensitivities far away from sources and receivers are small.

There are also some characteristic differences between these two applications. For example, in electromagnetic cross-borehole tomography, the sources and receivers are typically not located at the boundaries of the imaging domain, such that sidelobes of the sensitivity functions, which occur beyond the region of interest, have to be taken into account as well in the imaging process. Moreover, the propagating fields are now vector fields rather than scalar fields. This gives us a richer variety of sensitivity functions, changing with the component of the fields which is used for collecting the data.

We will see in this paper that the shapes of the sensitivity functions in EMIT show more variations than in optical tomography. For certain source-receiver geometries, the sensitivities in the region of interest are also here mainly concentrated on some almost 'banana-shaped' regions, whereas for other source-receiver configurations these regions look more like 'elongated doughnuts', with almost vanishing sensitivities close to the connecting line of source and receiver. We mention that another related geophysical application, which EMIT and OT are interesting to compare with, is hydrology. That situation is treated in more details for example in Vasco *et al* [45].

The single-step adjoint field inversion method which we are presenting here can be viewed as a nonlinear generalization of the algebraic reconstruction technique (ART) in x-ray tomography [33, 36]. In contrary to the filtered backprojection method mentioned earlier, ART uses only part of the data in each step of the reconstruction. It is an iterative technique and applies successive corrections to some initial guess for the parameter distribution, which in x-ray tomography is the *attenuation*. Each of these corrections is calculated by 'backprojecting' a (preprocessed or filtered) part of the residuals along those straight lines into the imaging domain which correspond to the incoming direction of the probing x-rays. We will show that, in an analogous way, each individual backprojection step of our generalized ART algorithm for EMIT takes place along sensitivity functions. An important difference of our generalized ART scheme to the classical ART algorithm is its nonlinearity. Whereas the sensitivities in the classical ART method are always concentrated on the same straight lines, the shapes of our sensitivity functions change with each update. The final reconstruction of our inversion method is given as a superposition of sensitivity functions with weights determined by the residual values which

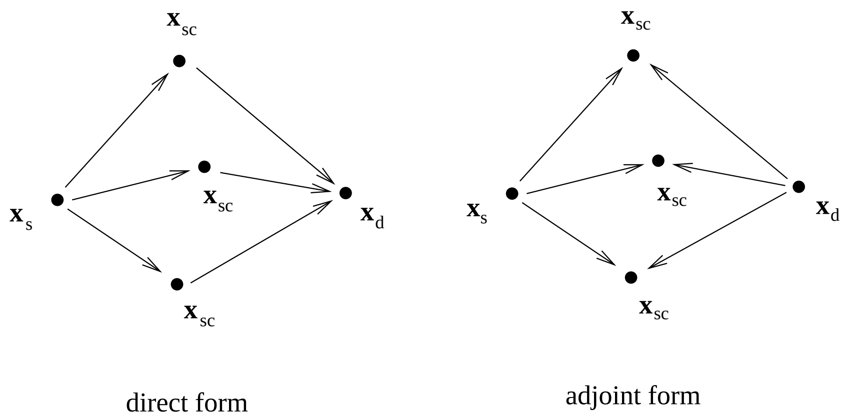

Figure 1: Feynman diagrams visualizing direct and adjoint forms of sensitivity functions. $\mathbf{x}_s$ source position, $\mathbf{x}_d$ receiver position, $\mathbf{x}_{sc}$ scattering points.

appear during the reconstruction process. The knowledge of the general stucture of the sensitivity functions during the reconstruction process provides us with useful information about the resolution which we can expect from the final reconstruction.

In this paper we make use of the so-called 'adjoint method' for calculating sensitivity functions. It has been pointed out several times in the literature that in parameter estimation problems where the number of unknown parameters becomes large, this adjoint method can be much less computationally expensive than the 'direct method' for calculating sensitivity relations. See for example [4, 5, 7, 16, 23, 25, 27, 31, 32, 35, 38, 40, 42]. This is in particular true in cases where the Green functions of the underlying forward problem (for example Maxwell's equations) are not known analytically, and have to be evaluated by employing some numerical forward modelling code. Given a source and a receiver position for which we want to calculate the space-dependent sensitivity functions, the 'direct method' would require us to make a separate run of this forward modelling code for each scattering point in the medium. In a large scale inversion problem like ours, this would mean to solve 10^5–10^6 forward problems in order to find one sensitivity function. The 'adjoint method' requires only the calculation of one forward and one adjoint problem in order to calculate the same sensitivity function. The Feynman diagrams in Figure 1 visualize this relationship. Each knot in the figure where one or more arrows originate indicates a separate run of the forward modelling code. In situations where we are interested in calculating the sensitivity functions only for a small number of sources and receivers but a large number of scattering points, the adjoint method is therefore by far more efficient than the direct method.

Sensitivity functions are closely related to Fréchet derivatives, which are evaluated at some reference parameter distribution. They describe the amount by which the receiver measurements will change if we slightly perturb the given reference parameter distribution at a certain position in the medium. Our linearized residual operator is just the Fréchet derivative of the nonlinear residual operator. We want to mention, however, that actually proving Fréchet differentiability of the nonlinear residual operator is not an easy task, and is beyond the scope of this paper. A possible method of proving Fréchet differentiability for general bilinear inverse problems can be found in [19]. We also mention that Fréchet differentiability for a related 3D-Maxwell problem has been discussed recently in [3].

Assuming that our residual operator is differentiable, we will show that the sensitivity functions decompose this linearized residual operator as well as its adjoint operator. In many applications, in particular if the starting point is the discretized model of the forward problem, this Fréchet derivative is called the 'Jacobian' or 'sensitivity matrix' of the underlying forward operator. The sensitivity functions can then be interpreted as the rows (or columns) of the Jacobian or sensitivity matrix. They play a major role in basically all gradient-based inversion methods which try to minimize the least squares measure of the misfit between given data and predicted data corresponding to a reference medium. Therefore, the results which are presented here might also be useful beyond the single step adjoint field inversion method which we will concentrate on in the following.

The paper is organized as follows. In section 2 we present the basic equations of EMs in a form convenient for development of the adjoint technique. In section 3, we define the function spaces and inner products which will be used in this paper, and derive expressions for the linearized residual operator. Expressions for the adjoint linearized residual operator are derived in section 4. The basic decomposition of these two operators in anisotropic sensitivity functions is then given in section 5.1 and proven in section 5.2. The corresponding isotropic forms are subject of section 6. In section 7 we generalize the single step adjoint field method presented in [22] to the situation of anisotropic media. Section 8 describes the numerical experiments which we have performed, and section 9 discusses these results and gives some conclusions and possible directions for future research.

2 Maxwell's equations for anisotropic media

We consider the system of time-harmonic Maxwell's Equations in three spatial dimensions

$$\nabla \times \mathbf{H}(\mathbf{x}) - (i\omega\epsilon(\mathbf{x}) + \sigma(\mathbf{x}))\,\mathbf{E}(\mathbf{x}) = \mathbf{J}(\mathbf{x}), \tag{1}$$

$$\nabla \times \mathbf{E}(\mathbf{x}) + i\omega\mu(\mathbf{x})\,\mathbf{H}(\mathbf{x}) = \mathbf{M}(\mathbf{x}), \tag{2}$$

$$\nabla \cdot \epsilon\mathbf{E}(\mathbf{x}) = 0, \qquad \nabla \cdot \mu\mathbf{H}(\mathbf{x}) = 0, \tag{3}$$

where $\mathbf{E}(\mathbf{x})$ and $\mathbf{H}(\mathbf{x})$ denote the electric and magnetic field, $\mathbf{J}(\mathbf{x})$ and $\mathbf{M}(\mathbf{x})$ are the electric and magnetic source currents, $\omega > 0$ is the angular frequency, $\omega = 2\pi f$, and $i = \sqrt{-1}$. The parameters describing the underlying medium are the electric conductivity $\sigma(\mathbf{x})$ with the dimension Siemens per metre (S/m), the dielectric permittivity

$\epsilon(\mathbf{x})$ having dimension Farad per metre (F/m), and the magnetic permeability $\mu(\mathbf{x})$ with the dimension Henry per metre (H/m). We assume that all these parameters are strictly positive in the physical domain $\sigma(\mathbf{x}) > 0$, $\epsilon(\mathbf{x}) > 0$, and $\mu(\mathbf{x}) > 0$ in $\mathbb{R}^3$. Equations (3) indicate that there are no electric or magnetic space charges in the medium.

In an earlier paper Dorn *et al.* [22] we considered the case where all physical parameters of the medium are isotropic. In that case the physical parameters are described by (complex valued) scalar functions. For anisotropic media these have to be replaced by general 3×3 tensor functions. To simplify our derivation, however, we will assume in the following (without loss of generality) that $\sigma(\mathbf{x})$, $\epsilon(\mathbf{x})$, and $\mu(\mathbf{x})$ are described by diagonal tensors with real positive numbers on the diagonal and zero off-diagonal elements. We get the representations

$$\begin{aligned}
\sigma(\mathbf{x}) &= \mathbf{diag}(\sigma^{(x)}(\mathbf{x}), \sigma^{(y)}(\mathbf{x}), \sigma^{(z)}(\mathbf{x})), \\
\epsilon(\mathbf{x}) &= \mathbf{diag}(\epsilon^{(x)}(\mathbf{x}), \epsilon^{(y)}(\mathbf{x}), \epsilon^{(z)}(\mathbf{x})), \\
\mu(\mathbf{x}) &= \mathbf{diag}(\mu^{(x)}(\mathbf{x}), \mu^{(y)}(\mathbf{x}), \mu^{(z)}(\mathbf{x})).
\end{aligned} \tag{4}$$

For the following, we introduce the notation

$$a = i\omega\mu, \qquad b = i\omega\epsilon + \sigma, \tag{5}$$

with

$$\begin{aligned}
a(\mathbf{x}) &= \mathbf{diag}(a^{(x)}(\mathbf{x}), a^{(y)}(\mathbf{x}), a^{(z)}(\mathbf{x})), \\
b(\mathbf{x}) &= \mathbf{diag}(b^{(x)}(\mathbf{x}), b^{(y)}(\mathbf{x}), b^{(z)}(\mathbf{x})).
\end{aligned}$$

With the notation of (5) we write (1),(2) as

$$\nabla \times \mathbf{H}(\mathbf{x}) - b(\mathbf{x})\,\mathbf{E}(\mathbf{x}) = \mathbf{J}(\mathbf{x}), \tag{6}$$

$$\nabla \times \mathbf{E}(\mathbf{x}) + a(\mathbf{x})\,\mathbf{H}(\mathbf{x}) = \mathbf{M}(\mathbf{x}). \tag{7}$$

This is the form of Maxwell's equations that we will use.

Equations (6),(7) describe the propagation of an electromagnetic field which is generated by a (time-harmonic) source distribution

$$\tilde{\mathbf{q}}(\mathbf{x}, t) = \mathbf{q}(\mathbf{x})e^{i\omega t} = \begin{pmatrix} \mathbf{J}(x) \\ \mathbf{M}(x) \end{pmatrix} e^{i\omega t},$$

where we typically will apply a magnetic dipole source of the form

$$\mathbf{q}(\mathbf{x}) = \begin{pmatrix} \mathbf{0} \\ \mathbf{m_s}\delta(\mathbf{x} - \mathbf{s}) \end{pmatrix}. \tag{8}$$

Here, $\mathbf{m}_s$ is the magnetic dipole moment of the source and $\mathbf{s}$ the source position. In the following we consider (6),(7) in the unbounded domain $\Omega = \mathbb{R}^3$ for a given source (8). In section 7, we will extend the analysis to the case when data corresponding to many source positions are used.

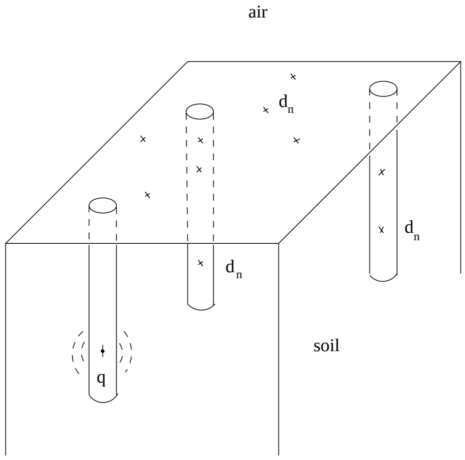

Figure 2: The figure shows a possible experimental setup. Three boreholes surround the area of interest. A z-directed dipole transmitter $\mathbf{q}$ is deployed in one of the boreholes, and data are gathered in the other boreholes and at the surface at positions $\mathbf{d}_n$, $n = 1, \ldots, N$. From these data, we want to recover the (anisotropic) conductivity and permittivity distribution in the earth.

We assume that equations (6),(7) provide a model for the propagation of the radiation caused by the source $\mathbf{q}$, and we measure the magnetic component of the field $\mathbf{H}(\mathbf{d}_n)$ for N discrete detector positions $\mathbf{d}_n$, $n = 1, \ldots, N$. In geophysical applications, it is often the case that the coefficient a does not vary significantly in the region of interest. In this paper, we will therefore assume that a is known in the whole domain Ω. In our numerical experiments, we will furthermore only consider the case that a is constant everywhere, although the discussion of the paper applies to the more general situation of space dependent parameters $a(x)$. The coefficient b is assumed to be unknown in the medium and has to be recovered from the data. The inverse problem we consider here is therefore as follows.

Inverse Problem: Assume that for many source distributions $\mathbf{q}_j = (\mathbf{J}_j, \mathbf{M}_j)^T$, $j = 1, \ldots, p$, for example of the form (8), the corresponding magnetic fields $\mathbf{H}_j(\mathbf{d}_n)$ are measured at the receiver locations $\mathbf{d}_n$, $n = 1 \ldots, N$. Find a parameter distribution $\tilde{b}$ such that for the solutions $(\tilde{\mathbf{E}}_j, \tilde{\mathbf{H}}_j)^T$ of

$$\nabla \times \tilde{\mathbf{H}}_j - \tilde{b}\,\tilde{\mathbf{E}}_j = \mathbf{J}_j, \tag{9}$$

$$\nabla \times \tilde{\mathbf{E}}_j + a\,\tilde{\mathbf{H}}_j = \mathbf{M}_j, \tag{10}$$

the magnetic field values at the receiver positions coincide with the data.

If there is no noise in the data then there may be many parameter distributions $\tilde{b}$ that satisfy (9), (10), so we have to select one using a regularization criterion. If there is noise, the usual case, then (9), (10) can be satisfied only in the sense of minimizing the sum of the squares of the differences between the two sides.

An efficient scheme for inverting the given data for the parameters b was presented in [22] for the case of isotropic media. In the present paper, we want to investigate a similar scheme if applied to anisotropic media. In particular, we will investigate the linearized residual operator and its adjoint for the given problem.

3 The residual operator and the linearized residual operator

We now define the basic function spaces which are used throughout this paper. The main objective of this section is to introduce the inner products which will be used in the derivation of the adjoint of the linearized residual operator which is discussed in section 4. The basic spaces which we will need are as follows.

$$
\begin{aligned}
F &= \left\{ b = \mathbf{diag}\left(b^{(x)}, b^{(y)}, b^{(z)}\right) \; ; \; b^{(x)}, b^{(y)}, b^{(z)} \in L^2(\Omega) \right\}, \\
Z &= \left\{ \zeta = (\mathbf{h}_1, \dots, \mathbf{h}_N), \quad \mathbf{h}_n \in \mathbb{C}^3 \right\}, \\
U &= \left\{ \begin{pmatrix} \mathbf{E}(\mathbf{x}) \\ \mathbf{H}(\mathbf{x}) \end{pmatrix} \; ; \; \mathbf{E}, \mathbf{H} \in [L^2(\Omega)]^3 \right\}, \\
Y &= \left\{ \begin{pmatrix} \mathbf{J}(\mathbf{x}) \\ \mathbf{M}(\mathbf{x}) \end{pmatrix} \; ; \; \mathbf{J}, \mathbf{M} \in [L^2(\Omega)]^3 \right\}.
\end{aligned}
$$

Here, F is the space of parameters, Z the space of the data or measurements, U the space of states, and Y the space of sources. All physical quantities considered here carry a physical dimension, which has to be taken into account when introducing the following inner products for these spaces.

$$
\left\langle \begin{pmatrix} \mathbf{E}_1 \\ \mathbf{H}_1 \end{pmatrix}, \begin{pmatrix} \mathbf{E}_2 \\ \mathbf{H}_2 \end{pmatrix} \right\rangle_U = \int_\Omega \gamma_E^2 \mathbf{E}_1 \overline{\mathbf{E}_2} \, d\mathbf{x} + \int_\Omega \gamma_H^2 \mathbf{H}_1 \overline{\mathbf{H}_2} \, d\mathbf{x},
$$

$$
\left\langle \begin{pmatrix} \mathbf{J}_1 \\ \mathbf{M}_1 \end{pmatrix}, \begin{pmatrix} \mathbf{J}_2 \\ \mathbf{M}_2 \end{pmatrix} \right\rangle_Y = \int_\Omega \gamma_J^2 \mathbf{J}_1 \overline{\mathbf{J}_2} \, d\mathbf{x} + \int_\Omega \gamma_M^2 \mathbf{M}_1 \overline{\mathbf{M}_2} \, d\mathbf{x},
$$

$$
\langle \zeta_1 \, , \, \zeta_2 \rangle_Z = \sum_{n=1}^{N} \gamma_H^2 \mathbf{h}_{1,n} \overline{\mathbf{h}_{2,n}} = \sum_{n=1}^{N} \sum_{i=x,y,z} \gamma_H^2 h_{1,n}^{(i)} \overline{h_{2,n}^{(i)}}
$$

with $\zeta_l = (\mathbf{h}_{l,1}, \dots, \mathbf{h}_{l,N})$, $\hat{\mathbf{h}}_{l,n} := \gamma_H \mathbf{h}_{l,n} \in \mathbb{C}^3$ for $l = 1, 2$, $n = 1, \dots, N$.

$$
\begin{aligned}
&\left\langle \mathbf{diag}(b_1^{(x)}, b_1^{(y)}, b_1^{(z)}) \, , \, \mathbf{diag}(b_2^{(x)}, b_2^{(y)}, b_2^{(z)}) \right\rangle_F \\
&\qquad = \int_\Omega \gamma_b^2 \left(b_1^{(x)}(\mathbf{x}) \overline{b_2^{(x)}(\mathbf{x})} + b_1^{(y)}(\mathbf{x}) \overline{b_2^{(y)}(\mathbf{x})} + b_1^{(z)}(\mathbf{x}) \overline{b_2^{(z)}(\mathbf{x})} \right) d\mathbf{x}.
\end{aligned}
$$

The constants γ_E, γ_H, γ_J, γ_M and γ_b are introduced in order to make the given scalar products dimensionless. More precisely, we have $\gamma_E = [\mathbf{E}]^{-1}$, $\gamma_H = [\mathbf{H}]^{-1}$,

$\gamma_J = [\mathbf{J}]^{-1}$, $\gamma_M = [\mathbf{M}]^{-1}$, and $\gamma_b = [b]^{-1}$, where the symbol [.] denotes the dimension of the corresponding physical quantity. Notice that $\gamma_b \gamma_E = \gamma_J$, which follows immediately from (6). We will also consider in this paper the corresponding dimensionless quantities which we always indicate by a roof on top of the symbol, for example $\hat{b} = \gamma_b b$ for $b \in F$ or $\hat{\mathbf{h}} = \gamma_H \mathbf{h}$ for $\mathbf{h} \in Z$. For these quantities, we will accordingly use the inner products $\langle\,,\,\rangle_{\hat{F}}$, $\langle\,,\,\rangle_{\hat{Z}}$, ..., which are defined as above but without the additional factors in the integrals. The spaces F, U, Y and Z (as well as $\hat{F}$, $\hat{U}$, $\hat{Y}$ and $\hat{Z}$) are Hilbert spaces with these inner products.

We write equations (6),(7) in system form

$$\Lambda_M(b)\,\mathbf{u} \;=\; \mathbf{q}, \tag{11}$$

with

$$\Lambda_M(b) \;=\; \begin{pmatrix} -b & \nabla\times \\ \nabla\times & a \end{pmatrix}, \tag{12}$$

and

$$\mathbf{u} = \begin{pmatrix} \mathbf{E} \\ \mathbf{H} \end{pmatrix}, \qquad \mathbf{q} = \begin{pmatrix} \mathbf{J} \\ \mathbf{M} \end{pmatrix}.$$

The Maxwell Operator $\Lambda_M(b)$ is defined on a dense subset of the Hilbert space U, given the parameter distribution b. When the conductivity is everywhere positive, $\sigma > 0$, (11) has a unique solution $\mathbf{u} \in U$ for each source $\mathbf{q} \in Y$. For a function $\mathbf{u} \in U$ of (11) we define the *measurement operator* $M : U \to Z$ by

$$\left(M\mathbf{u}\right)_n(\mathbf{x}) \;=\; \int_\Omega \delta(\mathbf{x} - \mathbf{d}_n)\,\mathbf{H}(\mathbf{x})\,d\mathbf{x} \qquad (n = 1, \ldots, N) \tag{13}$$

with $\mathbf{u} = \begin{pmatrix} \mathbf{E} \\ \mathbf{H} \end{pmatrix}$, and with $\mathbf{d}_n$, $n = 1, \ldots, N$, being the detector positions. The measurement operator M is well defined by (13) and maps the fields $\mathbf{u} \in U$ to a vector of complex numbers $M\mathbf{u} \in Z$, which consists of point measurements of the magnetic field components at the detector positions $\mathbf{d}_n$, $n = 1, \ldots, N$. More precisely, we can write

$$M \begin{pmatrix} \mathbf{E} \\ \mathbf{H} \end{pmatrix} \;=\; \left(\mathbf{H}(\mathbf{d}_1), \mathbf{H}(\mathbf{d}_2), \ldots, \mathbf{H}(\mathbf{d}_N)\right)^T,$$

where the symbol ^{T} stands for transpose. For the given source $\mathbf{q}$ and given data $g \in Z$ we define the *residual operator* R by

$$R : F \to Z, \qquad R(b) \;=\; M\mathbf{u}(b) \;-\; g,$$

where $\mathbf{u}(b)$ is the solution of (11) with parameter b. The operator R is a *nonlinear* operator from the space of parameters F to the space of measurements Z.

We will assume that the source $\mathbf{q}$ is given by (8) with

$$\mathbf{m}_s \;=\; \alpha_1 \mathbf{e}_1 + \alpha_2 \mathbf{e}_2 + \alpha_3 \mathbf{e}_3, \tag{14}$$

with $\hat{\alpha}_i := \gamma_M \alpha_i \in \mathbb{C}$ for $i = 1, 2, 3$. The symbols $\mathbf{e}_i$, $i = 1, 2, 3$, will always denote the cartesian unit vectors, for example $\mathbf{e}_1 = (1, 0, 0)^T$. We will also often replace $i = 1, 2, 3$ by $i = x, y, z$ in the notation in order to emphasize the spatial dimension which we refer to. We denote by $\mathbf{E}(\mathbf{x}) = (E^{(x)}(\mathbf{x}), E^{(y)}(\mathbf{x}), E^{(z)}(\mathbf{x}))^T$ (and similarly $\mathbf{H}(\mathbf{x})$) the solution of the *forward problem*

$$\Lambda_M(b) \begin{pmatrix} \mathbf{E} \\ \mathbf{H} \end{pmatrix} = \begin{pmatrix} 0 \\ \mathbf{m}_s \delta(\mathbf{x} - \mathbf{s}) \end{pmatrix} \tag{15}$$

with $\Lambda_M(b)$ defined as in (12), and a, b defined as in (5). In order to find a useful representation of the *linearized residual operator* R' of R, we perturb b, $\mathbf{E}$ and $\mathbf{H}$ by

$$b \to b + \delta b \qquad \mathbf{E} \to \mathbf{E} + \mathbf{v} \qquad \mathbf{H} \to \mathbf{H} + \mathbf{w},$$

and plug this into (6),(7). When neglecting terms of higher than linear order in δb, v and w, and applying the measurement operator M, we arrive at the following result.

Theorem 3.1 *The linearized residual operator $R'[b]$ is given by*

$$R'[b]\,\delta b = M \begin{pmatrix} \mathbf{v} \\ \mathbf{w} \end{pmatrix}, \tag{16}$$

where $\binom{\mathbf{v}}{\mathbf{w}}$ solves

$$\Lambda_M(b) \begin{pmatrix} \mathbf{v} \\ \mathbf{w} \end{pmatrix} = \begin{pmatrix} \delta b\, \mathbf{E} \\ 0 \end{pmatrix}. \tag{17}$$

4 The adjoint linearized residual operator

The *adjoint linearized residual operator* $R'[b]^*$ is formally defined by the identity

$$\left\langle R'[b]\,\delta b\,,\,\zeta \right\rangle_Z = \left\langle \delta b\,,\, R'[b]^* \zeta \right\rangle_F.$$

It is a mapping from the data space Z into the parameter space F. In the next theorem, we will present a useful expression for the action of $R'[b]^*$ on a given vector $\zeta \in Z$.

Theorem 4.1 *Let us assume that we are given $\zeta = (\mathbf{h}_1, \ldots, \mathbf{h}_N) \in Z$ with $\hat{\mathbf{h}}_n = (\hat{h}_n^{(x)}, \hat{h}_n^{(y)}, \hat{h}_n^{(z)})^T \in \mathbb{C}^3$ for $n = 1, \ldots, N$. Furthermore, we denote by $\mathcal{E}(\mathbf{x}) = (\mathcal{E}^{(x)}(\mathbf{x}), \mathcal{E}^{(y)}(\mathbf{x}), \mathcal{E}^{(z)}(\mathbf{x}))^T$ the solution of the adjoint problem*

$$\Lambda_M^*(b) \begin{pmatrix} \mathcal{E} \\ \mathcal{H} \end{pmatrix} = \begin{pmatrix} 0 \\ \gamma_M^{-1} \sum_{n=1}^N \sum_{i=x,y,z} \hat{h}_n^{(i)} \mathbf{e}_i \delta(\mathbf{x} - \mathbf{d}_n) \end{pmatrix}, \tag{18}$$

with

$$\Lambda_M^*(b) = \begin{pmatrix} -\bar{b} & \nabla \times \\ \nabla \times & \bar{a} \end{pmatrix}, \tag{19}$$

$$\overline{b} = -i\omega\epsilon + \sigma, \quad \overline{a} = -i\omega\mu.$$

Then $R'[b]^*\zeta \in F$ *is given by*

$$\left(R'[b]^*\zeta\right)(\mathbf{x}) = \gamma_b^{-1}\mathbf{diag}\left(\overline{\hat{E}^{(x)}(\mathbf{x})}\hat{\mathcal{E}}^{(x)}(\mathbf{x}),\, \overline{\hat{E}^{(y)}(\mathbf{x})}\hat{\mathcal{E}}^{(y)}(\mathbf{x}),\, \overline{\hat{E}^{(z)}(\mathbf{x})}\hat{\mathcal{E}}^{(z)}(\mathbf{x})\right), \tag{20}$$

where $\mathbf{E}$ *is the solution of (15).*

The proof of this theorem is given next.

Let $\binom{\mathbf{v}}{\mathbf{w}}, \binom{\mathcal{E}}{\mathcal{H}} \in U$. Using Green's formulas for an infinite space, without boundary terms since $\sigma > 0$ everywhere, we have

$$\begin{aligned}\int_\Omega (\nabla \times \mathbf{w}) \cdot \bar{\mathcal{H}}\, d\mathbf{x} &= \int_\Omega \mathbf{w} \cdot \overline{(\nabla \times \mathcal{H})}\, d\mathbf{x},\\ \int_\Omega (\nabla \times \mathbf{v}) \cdot \bar{\mathcal{E}}\, d\mathbf{x} &= \int_\Omega \mathbf{v} \cdot \overline{(\nabla \times \mathcal{E})}\, d\mathbf{x},\end{aligned}$$

such that

$$\left\langle \Lambda_M(b)\begin{pmatrix}\mathbf{v}\\ \mathbf{w}\end{pmatrix}, \begin{pmatrix}\mathcal{E}\\ \mathcal{H}\end{pmatrix}\right\rangle_{L^2} = \tag{21}$$

$$\begin{aligned}&\int_\Omega \gamma_J\gamma_E(\nabla \times \mathbf{w} - b\mathbf{v}) \cdot \bar{\mathcal{E}}\, d\mathbf{x} + \int_\Omega \gamma_M\gamma_H(\nabla \times \mathbf{v} + a\mathbf{w}) \cdot \bar{\mathcal{H}}\, d\mathbf{x}\\ &= \int_\Omega \gamma_J\gamma_E \mathbf{v} \cdot \overline{(\nabla \times \mathcal{H} - \bar{b}\mathcal{E})}\, d\mathbf{x} + \int_\Omega \gamma_M\gamma_H \mathbf{w} \cdot \overline{(\nabla \times \mathbf{E} + \bar{a}\mathcal{H})}\, d\mathbf{x}\\ &= \left\langle \begin{pmatrix}\mathbf{v}\\ \mathbf{w}\end{pmatrix}, \Lambda_M^*(b)\begin{pmatrix}\mathcal{E}\\ \mathcal{H}\end{pmatrix}\right\rangle_{L^2}\end{aligned}$$

with $\Lambda_M^*(b)$ defined as in (19). We need furthermore the identity

$$\int_\Omega \mathbf{w}(\mathbf{x})\,\overline{\left[\sum_{n=1}^N \sum_{i=x,y,z} h_n^{(i)}\mathbf{e}_i\delta(\mathbf{x} - \mathbf{d}_n)\right]}\, d\mathbf{x} = \sum_{n=1}^N \sum_{i=x,y,z} \left(\int_\Omega \mathbf{w}(\mathbf{x})\delta(\mathbf{x} - \mathbf{d}_n)\, d\mathbf{x}\right)\overline{h_n^{(i)}}\mathbf{e}_i. \tag{22}$$

Combining (21),(22) yields

$$\begin{aligned}&\left\langle \Lambda_M(b)\begin{pmatrix}\mathbf{v}\\ \mathbf{w}\end{pmatrix}, \begin{pmatrix}\mathcal{E}\\ \mathcal{H}\end{pmatrix}\right\rangle_{L^2} + \int_\Omega \gamma_H\gamma_M \mathbf{w}(\mathbf{x})\,\overline{\left[\gamma_H\gamma_M^{-1}\sum_{n=1}^N \sum_{i=x,y,z} h_n^{(i)}\mathbf{e}_i\delta(\mathbf{x} - \mathbf{d}_n)\right]}\, d\mathbf{x}\\ &= \left\langle \begin{pmatrix}\mathbf{v}\\ \mathbf{w}\end{pmatrix}, \Lambda_M^*(b)\begin{pmatrix}\mathcal{E}\\ \mathcal{H}\end{pmatrix}\right\rangle_{L^2} + \gamma_H^2 \sum_{n=1}^N \sum_{i=x,y,z} \left(\int_\Omega \mathbf{w}(\mathbf{x})\delta(\mathbf{x} - \mathbf{d}_n)\, d\mathbf{x}\right)\overline{h_n^{(i)}}\mathbf{e}_i\end{aligned} \tag{23}$$

Now let $\binom{\mathbf{v}}{\mathbf{w}}$ be the solution of (17), $\binom{\mathbf{E}}{\mathbf{H}}$ the solution of (15), and $\binom{\mathcal{E}}{\mathcal{H}}$ the solution of (18). Then the second term on the left hand side of (23) and the first term on the right hand side of (23) cancel each other. The second term on the right hand side of (23) can be written as

$$\left\langle M\begin{pmatrix}\mathbf{v}\\ \mathbf{w}\end{pmatrix}, \zeta\right\rangle_Z,$$

whereas the first term on the left hand side is equal to

$$\left\langle \begin{pmatrix} \delta b\mathbf{E} \\ 0 \end{pmatrix}, \begin{pmatrix} \mathcal{E} \\ \mathcal{H} \end{pmatrix} \right\rangle_{L^2} = \int_\Omega \gamma_b \gamma_E^2 \Big(\delta b^{(x)} E^{(x)}, \delta b^{(y)} E^{(y)}, \delta b^{(z)} E^{(z)} \Big) \cdot \overline{\mathcal{E}}\, d\mathbf{x}$$

$$\begin{aligned} &= \int_\Omega \gamma_b \gamma_E^2 \Big\{ \delta b^{(x)} \Big[E^{(x)} \overline{\mathcal{E}^{(x)}} \Big] + \delta b^{(y)} \Big[E^{(y)} \overline{\mathcal{E}^{(y)}} \Big] + \delta b^{(z)} \Big[E^{(z)} \overline{\mathcal{E}^{(z)}} \Big] \Big\}\, d\mathbf{x} \\ &= \Big\langle \delta b, \gamma_b^{-1} \mathbf{diag} \Big(\overline{\hat{E}^{(x)}(\mathbf{x})} \hat{\mathcal{E}}^{(x)}(\mathbf{x}), \overline{\hat{E}^{(y)}(\mathbf{x})} \hat{\mathcal{E}}^{(y)}(\mathbf{x}), \overline{\hat{E}^{(z)}(\mathbf{x})} \hat{\mathcal{E}}^{(z)}(\mathbf{x}) \Big) \Big\rangle_F . \end{aligned}$$

Thus (23) can be written as

$$\Big\langle R'(b)\, \delta b, \zeta \Big\rangle_Z = \Big\langle \delta b, R'(b)^* \zeta \Big\rangle_F$$

with $R'(b)^*\zeta$ defined by (20). This proves Theorem 4.1 $\square$

5 Adjoint sensitivity analysis for anisotropic media

5.1 Decomposition of the residual operator and its adjoint

In this section, we will present the basic decompositions of the linearized residual operator and its adjoint into sensitivity functions.

Theorem 5.1 *Given a source (14). We can find functions $\Phi^{(i)}(n,l;\mathbf{y})$ and $S_k^{(i)}(n,l;\mathbf{y})$, $i = 1,2,3$, such that the linearized residual operator $R'[b]$ can be decomposed as*

$$\begin{aligned} \Big(R'[b]\delta b \Big)_n &= \gamma_H^{-1} \sum_{l=1}^{3} \left(\sum_{i=1}^{3} \int_\Omega \widehat{\delta b}^{(i)}(\mathbf{y})\, \Phi^{(i)}(n,l;\mathbf{y}) d\mathbf{y} \right) \mathbf{e}_l \qquad (24) \\ &= \gamma_H^{-1} \sum_{l=1}^{3} \left(\sum_{i=1}^{3} \int_\Omega \widehat{\delta b}^{(i)}(\mathbf{y}) \Big(\sum_{k=1}^{3} \hat{\alpha}_k\, S_k^{(i)}(n,l;\mathbf{y}) \Big) d\mathbf{y} \right) \mathbf{e}_l . \end{aligned}$$

Moreover, the same functions $\Phi^{(i)}(n,l;\mathbf{y})$ and $S_k^{(i)}(n,l;\mathbf{y})$ also decompose the adjoint linearized residual operator $R'[b]^*$ in the following way

$$\begin{aligned} \Big(R'[b]^* \zeta \Big)^{(i)}(\mathbf{y}) &= \gamma_b^{-1} \sum_{n=1}^{N} \sum_{l=1}^{3} \hat{h}_n^{(l)} \overline{\Phi^{(i)}(n,l;\mathbf{y})} \qquad (25) \\ &= \gamma_b^{-1} \sum_{n=1}^{N} \sum_{l=1}^{3} \hat{h}_n^{(l)} \left(\sum_{k=1}^{3} \overline{\hat{\alpha}_k S_k^{(i)}(n,l;\mathbf{y})} \right). \end{aligned}$$

The functions $\Phi^{(i)}(n,l;\mathbf{y})$ and $S_k^{(i)}(n,l;\mathbf{y})$ are called (source-dependent and source-independent, respectively,) anisotropic sensitivity functions.

In the following, we will first define these sensitivity functions $S_k^{(i)}(n,l;\mathbf{y})$ and $\Phi^{(i)}(n,l;\mathbf{y})$, and then reformulate the above theorem in a slightly more formal way. First, we decompose the given vector $\zeta = (\mathbf{h}_1,\dots,\mathbf{h}_N) \in Z$ as

$$\mathbf{h}_n \;=\; h_n^{(1)}\mathbf{e}_1 + h_n^{(2)}\mathbf{e}_2 + h_n^{(3)}\mathbf{e}_3 \tag{26}$$

with $\hat{h}_n^{(i)} := \gamma_H h_n^{(i)} \in \mathbb{C}$ for $i = 1,2,3$ and $n = 1,\dots,N$. Let $(\mathbf{E}_k,\mathbf{H}_k)^T$, $k = 1,2,3$, be the solutions of the direct problems

$$\Lambda_M(b)\begin{pmatrix}\mathbf{E}_k\\ \mathbf{H}_k\end{pmatrix} \;=\; \begin{pmatrix}0\\ \gamma_M^{-1}\mathbf{e}_k\delta(\mathbf{x}-\mathbf{s})\end{pmatrix}. \tag{27}$$

Moreover, let $(\mathcal{E}_{n,l},\mathcal{H}_{n,l})^T$, $l = 1,2,3$, $n = 1\dots,N$, be solutions of the adjoint problems

$$\Lambda_M^*(b)\begin{pmatrix}\mathcal{E}_{n,l}\\ \mathcal{H}_{n,l}\end{pmatrix} \;=\; \begin{pmatrix}0\\ \gamma_M^{-1}\mathbf{e}_l\delta(\mathbf{x}-\mathbf{d}_n)\end{pmatrix}, \tag{28}$$

where $\Lambda_M^*(b)$ is defined as in (19). With this notation, the *anisotropic sensitivity functions* $S_k^{(i)}(n,l;\mathbf{y})$ are defined by

$$S_k^{(i)}(n,l;\mathbf{y}) \;=\; \hat{E}_k^{(i)}(\mathbf{y})\,\overline{\hat{\mathcal{E}}_{n,l}^{(i)}(\mathbf{y})}, \tag{29}$$

and the *source dependent* anisotropic sensitivity functions $\Phi^{(i)}(n,l;\mathbf{y})$ by

$$\Phi^{(i)}(n,l;\mathbf{y}) \;=\; \hat{E}^{(i)}(\mathbf{y})\,\overline{\hat{\mathcal{E}}_{n,l}^{(i)}(\mathbf{y})} \;=\; \sum_{k=1}^{3}\hat{\alpha}_k\; S_k^{(i)}(n,l;\mathbf{y}), \tag{30}$$

where the fields $(\mathbf{E},\mathbf{H})^T$ are solutions of (15). Notice that these sensitivity functions are defined to be dimensionless.

Now, making use of the inner products which have been introduced in section 3, we get the following equivalent formulation of Theorem 5.1.

Theorem 5.2 *Given a source (14). Define the functions $\Phi^{(i)}(n,l;\mathbf{y})$ as in (30) and $S_k^{(i)}(n,l;\mathbf{y})$ as in (29). Then we have the following decompositions of the linearized residual operator $R'[b]$ and its adjoint $R'[b]^*$.*
Projection Step:

$$\begin{aligned}\left(R'[b]\delta b\right)_n \;&=\; \gamma_H^{-1}\sum_{l=1}^{3}\left(\sum_{i=1}^{3}\left\langle \widehat{\delta b}^{(i)}\,,\,\overline{\Phi^{(i)}(n,l;\,.\,)}\right\rangle_{\hat{F}}\right)\mathbf{e}_l \\ &=\; \gamma_H^{-1}\sum_{l=1}^{3}\left(\sum_{i=1}^{3}\sum_{k=1}^{3}\hat{\alpha}_k\left\langle \widehat{\delta b}^{(i)}\,,\,\overline{S_k^{(i)}(n,l;\,.\,)}\right\rangle_{\hat{F}}\right)\mathbf{e}_l.\end{aligned} \tag{31}$$

Backprojection Step:

$$\begin{aligned}\left(R'[b]^*\zeta\right)^{(i)}(\mathbf{y}) \;&=\; \gamma_b^{-1}\left\langle\hat{\zeta}\,,\,\Phi^{(i)}(\,.\,,\,.\,;\mathbf{y})\right\rangle_{\hat{Z}} \\ &=\; \gamma_b^{-1}\sum_{k=1}^{3}\hat{\alpha}_k\left\langle\hat{\zeta}\,,\,S_k^{(i)}(\,.\,,\,.\,;\mathbf{y})\right\rangle_{\hat{Z}}.\end{aligned} \tag{32}$$

Remark 5.1 *We note that equation (31) gives rise to the interpretation of $R^{'}[b]$ as a 'projection operator'. It 'projects' each component $\delta b^{(i)}$ of the parameter perturbation δb along the sensitivity function $\Phi^{(i)}(n, l;\ .\ )$ into the data space Z. Summing up all these contributions yields the (linearized) residuals $R^{'}[b]\delta b$. Analogously, equation (32) gives rise to the interpretation of $R^{'}[b]^*$ as a 'backprojection operator'. It 'backprojects' the residual vector ζ of the data space Z along the sensitivity functions $\Phi^{(i)}(\ .\ ,\ .\ ; \mathbf{y})$ into the parameter space F.*

5.2 Proof of Theorem 5.1

In this section, we will prove Theorem 5.1. To start with, Theorem 3.1 shows that the linearized residuals in the measurements at the detector positions $\mathbf{d}_n$ are given by

$$\left(R^{'}[b]\delta b\right)_n = \mathbf{w}(\mathbf{d}_n), \tag{33}$$

where $(\mathbf{v}, \mathbf{w})^T$ solves

$$\Lambda_M(b)\begin{pmatrix}\mathbf{v}\\ \mathbf{w}\end{pmatrix} = \begin{pmatrix}\delta b\,\mathbf{E}\\ 0\end{pmatrix}. \tag{34}$$

Let $(\mathbf{E}_k, \mathbf{H}_k)^T$ be the solution of (27). Using linearity of Maxwell's equations, we get with this notation

$$\mathbf{w}(\mathbf{d}_n) = \sum_{k=1}^{3} \hat{\alpha}_k \mathbf{w}_k(\mathbf{d}_n), \tag{35}$$

where $(\mathbf{v}_k, \mathbf{w}_k)^T$, $k = 1, 2, 3$, solve the linearized equations

$$\Lambda_M(b)\begin{pmatrix}\mathbf{v}_k\\ \mathbf{w}_k\end{pmatrix} = \begin{pmatrix}\delta b\mathbf{E}_k\\ 0\end{pmatrix}. \tag{36}$$

Let now $(\mathcal{E}_{n,l}, \mathcal{H}_{n,l})^T$, $l = 1, 2, 3$, $n = 1\ldots, N$, be the solution of (28). From (21) we have for general fields $(\mathbf{v}, \mathbf{w})^T, (\mathcal{E}, \mathcal{H})^T \in U$ the relation

$$\left\langle \Lambda_M(b)\begin{pmatrix}\mathbf{v}\\ \mathbf{w}\end{pmatrix}, \begin{pmatrix}\mathcal{E}\\ \mathcal{H}\end{pmatrix}\right\rangle_{L^2} = \left\langle \begin{pmatrix}\mathbf{v}\\ \mathbf{w}\end{pmatrix}, \Lambda_M^*(b)\begin{pmatrix}\mathcal{E}\\ \mathcal{H}\end{pmatrix}\right\rangle_{L^2}.$$

Applying this to the solutions of (28) and (36) we get

$$\left\langle \begin{pmatrix}\delta b\mathbf{E}_k\\ 0\end{pmatrix}, \begin{pmatrix}\mathcal{E}_{n,l}\\ \mathcal{H}_{n,l}\end{pmatrix}\right\rangle_{L^2} = \left\langle \begin{pmatrix}\mathbf{v}_k\\ \mathbf{w}_k\end{pmatrix}, \begin{pmatrix}0\\ \gamma_M^{-1}\mathbf{e}_l\delta(\mathbf{x}-\mathbf{d}_n)\end{pmatrix}\right\rangle_{L^2},$$

or, written explicitly

$$\int_\Omega \gamma_b\gamma_E^2\mathbf{E}_k(\mathbf{y})\delta b(\mathbf{y})\overline{\mathcal{E}_{n,l}(\mathbf{y})}\,d\mathbf{y} = \int_\Omega \gamma_H\gamma_M\mathbf{w}_k(\mathbf{x})\cdot\gamma_M^{-1}\mathbf{e}_l\delta(\mathbf{x}-\mathbf{d}_n)\,d\mathbf{x},$$

where $\overline{\mathcal{E}_{n,l}(\mathbf{y})}$ denotes the complex conjugate of $\mathcal{E}_{n,l}(\mathbf{y})$. By summing up all terms $k = 1, 2, 3$, and carrying out the integration on the right hand side, equation (35) gets the form

$$\gamma_H\mathbf{w}(\mathbf{d}_n)\cdot\mathbf{e}_l = \gamma_b\gamma_E^2\sum_{k=1}^{3}\hat{\alpha}_k\int_\Omega \mathbf{E}(\mathbf{y})\delta b(\mathbf{y})\overline{\mathcal{E}_{n,l}(\mathbf{y})}\,d\mathbf{y},$$

or

$$\mathbf{w}(\mathbf{d}_n) \;=\; \gamma_H^{-1}\gamma_b\gamma_E^2 \sum_{l=1}^{3}\sum_{k=1}^{3} \hat{\alpha}_k \Big(\int_\Omega \mathbf{E}_k(\mathbf{y})\delta b(\mathbf{y})\overline{\mathcal{E}_{n,l}(\mathbf{y})}\, d\mathbf{y} \Big)\, \mathbf{e}_l. \tag{37}$$

We consider the case of an anisotropic medium

$$\begin{aligned} b(\mathbf{y}) \;&=\; \mathbf{diag}\left(b^{(1)}(\mathbf{y}), b^{(2)}(\mathbf{y}), b^{(3)}(\mathbf{y})\right), \\ \delta b(\mathbf{y}) \;&=\; \mathbf{diag}\left(\delta b^{(1)}(\mathbf{y}), \delta b^{(2)}(\mathbf{y}), \delta b^{(3)}(\mathbf{y})\right). \end{aligned}$$

Equation (37) yields with (29) and (33) the representation

$$\begin{aligned} \left(R^{'}[b]\delta b\right)_n \;&=\; \gamma_H^{-1}\gamma_b\gamma_E^2 \sum_{l=1}^{3} \left(\sum_{k=1}^{3}\sum_{i=1}^{3} \hat{\alpha}_k \Big(\int_\Omega E_k^{(i)}(\mathbf{y})\delta b^{(i)}(\mathbf{y})\overline{\mathcal{E}_{n,l}^{(i)}(\mathbf{y})}\, d\mathbf{y} \Big) \right) \mathbf{e}_l \\ &=\; \gamma_H^{-1} \sum_{l=1}^{3} \left(\sum_{i=1}^{3} \int_\Omega \widehat{\delta b}^{(i)}(\mathbf{y}) \Big(\sum_{k=1}^{3} \hat{\alpha}_k\; S_k^{(i)}(n,l;\mathbf{y}) \Big) d\mathbf{y} \right) \mathbf{e}_l, \end{aligned}$$

which is just (24).

Next, we derive the decomposition of the adjoint linearized residual operator as given in Theorem 5.1. Let the vector $\zeta = (\mathbf{h}_1, \ldots, \mathbf{h}_N) \in Z$ be given as in (26). We want to calculate the action of the adjoint linearized residual operator $R^{'}[b]^*$ on ζ. Equation (20) yields

$$\left(R^{'}[b]^*\zeta\right)(\mathbf{y}) \;=\; \gamma_b^{-1}\gamma_E^2 \sum_{n=1}^{N} \mathbf{diag}\left(\overline{E^{(1)}(\mathbf{y})}\mathcal{E}_n^{(1)}(\mathbf{y})\,,\; \overline{E^{(2)}(\mathbf{y})}\mathcal{E}_n^{(2)}(\mathbf{y})\,,\; \overline{E^{(3)}(\mathbf{y})}\mathcal{E}_n^{(3)}(\mathbf{y})\right), \tag{38}$$

where the upper index ${}^{(i)}$ denotes as before the i-th component of the given vector. The fields $(\mathbf{E},\mathbf{H})^T$ in (38) are solutions of (15), and the fields $(\mathcal{E}_n,\mathcal{H}_n)^T$ are solutions of

$$\Lambda_M^*(b) \begin{pmatrix} \mathcal{E}_n \\ \mathcal{H}_n \end{pmatrix} \;=\; \begin{pmatrix} 0 \\ \gamma_M^{-1}\sum_{l=x,y,z} \hat{h}_n^{(l)}\mathbf{e}_l\delta(\mathbf{x}-\mathbf{d}_n) \end{pmatrix}.$$

Using the decompositions (14) and (26), we get from linearity

$$\mathbf{E}(\mathbf{y}) \;=\; \sum_{k=1}^{3} \hat{\alpha}_k\mathbf{E}_k(\mathbf{y}), \qquad \mathcal{E}_n(\mathbf{y}) \;=\; \sum_{l=1}^{3} \hat{h}_n^{(l)}\mathcal{E}_{n,l}(\mathbf{y}),$$

with $\mathbf{E}_k(\mathbf{y})$ and $\mathcal{E}_n(\mathbf{y})$ solutions of (27) and (28), respectively. Equation (38) yields for the i-th component of $R^{'}[b]^*\zeta$ the expression

$$\left(R^{'}[b]^*\zeta\right)^{(i)}(\mathbf{y}) \;=\; \gamma_b^{-1}\gamma_E^2 \sum_{n=1}^{N}\sum_{k=1}^{3}\sum_{l=1}^{3} \overline{\hat{\alpha}_k}\hat{h}_n^{(l)}\overline{E_k^{(i)}(\mathbf{y})}\mathcal{E}_{n,l}^{(i)}(\mathbf{y}).$$

Using (29), we get finally

$$\left(R^{'}[b]^*\zeta\right)^{(i)}(\mathbf{y}) \;=\; \gamma_b^{-1} \sum_{n=1}^{N}\sum_{l=1}^{3} \hat{h}_n^{(l)} \left(\sum_{k=1}^{3} \overline{\hat{\alpha}_k S_k^{(i)}(n,l;\mathbf{y})} \right),$$

which is just (25). □

6 A special case: isotropic media

Let us consider an isotropic medium, i.e., let $b_{\text{iso}}(\mathbf{y})$, $\delta b_{\text{iso}}(\mathbf{y})$ be given by

$$
\begin{aligned}
b_{\text{iso}}(\mathbf{y}) &= \mathbf{diag}\left(b^{(0)}(\mathbf{y}), b^{(0)}(\mathbf{y}), b^{(0)}(\mathbf{y})\right), \\
\delta b_{\text{iso}}(\mathbf{y}) &= \mathbf{diag}\left(\delta b^{(0)}(\mathbf{y}), \delta b^{(0)}(\mathbf{y}), \delta b^{(0)}(\mathbf{y})\right).
\end{aligned}
$$

We can replace the diagonal tensors for describing the parameters δb_{iso} and b_{iso} by the scalar functions $\delta b^{(0)}$, $b^{(0)}$, which live in the reduced function space $L^2(\mathbb{R}^3)$. The *isotropic sensitivity functions* $S_k(n,l;\mathbf{y})$ and $\Phi(n,l;\mathbf{y})$ are defined as

$$
S_k(n,l;\mathbf{y}) = \hat{\mathbf{E}}_k(\mathbf{y}) \cdot \overline{\hat{\mathcal{E}}_{n,l}(\mathbf{y})}, \qquad \Phi(n,l;\mathbf{y}) = \hat{\mathbf{E}}(\mathbf{y}) \cdot \overline{\hat{\mathcal{E}}_{n,l}(\mathbf{y})}, \tag{39}
$$

where $\mathbf{E}_k(\mathbf{y})$ solves (27), $\mathbf{E}(\mathbf{y})$ solves (15), and $\mathcal{E}_{n,l}(\mathbf{y})$ solves (28). Obviously, we have

$$
S_k(n,l;\mathbf{y}) = \sum_{i=1}^{3} S_k^{(i)}(n,l;y), \qquad \Phi(n,l;\mathbf{y}) = \sum_{i=1}^{3} \Phi^{(i)}(n,l;y). \tag{40}
$$

With these functions, we can formulate the analogous form of Theorem 5.1 for isotropic media. The proof of the following two theorems is completely analogous to the proof of Theorem 5.1 which was given in section 5.2, such that we will omit it here.

Theorem 6.1 *Given a source (14). Let the functions $S_k(n,l;\mathbf{y})$ and $\Phi(n,l;\mathbf{y})$ be defined as in (39). Then we have the following decompositions of $R'[b]$*

$$
\begin{aligned}
\left(R'[b]\delta b\right)_n &= \gamma_H^{-1} \sum_{l=1}^{3} \left(\sum_{k=1}^{3} \hat{\alpha}_k \int_\Omega \widehat{\delta b}(\mathbf{y}) S_k(n,l;\mathbf{y})\, d\mathbf{y} \right) \mathbf{e}_l \qquad (41) \\
&= \gamma_H^{-1} \sum_{l=1}^{3} \left(\int_\Omega \widehat{\delta b}(\mathbf{y}) \Phi(n,l;\mathbf{y})\, d\mathbf{y} \right) \mathbf{e}_l.
\end{aligned}
$$

In addition, $R'[b]^*$ can be decomposed as

$$
\begin{aligned}
\left(R'[b]^*\zeta\right)(\mathbf{y}) &= \gamma_b^{-1} \sum_{n=1}^{N} \sum_{l=1}^{3} \hat{h}_n^{(l)} \sum_{k=1}^{3} \overline{\hat{\alpha}_k S_k(n,l;\mathbf{y})} \qquad (42) \\
&= \gamma_b^{-1} \sum_{n=1}^{N} \sum_{l=1}^{3} \hat{h}_n^{(l)} \overline{\Phi(n,l;\mathbf{y})}.
\end{aligned}
$$

Using a more formal notation, this theorem can be reformulated as follows.

Theorem 6.2 *Given a source (14). Define the functions $\Phi(n,l;\mathbf{y})$ and $S_k(n,l;\mathbf{y})$ as in (39). Then, the linearized residual operator $R'[b]$ and its adjoint $R'[b]^*$ have*

the following decompositions.
Projection step:

$$\left(R^{'}[b]\delta b\right)_n = \gamma_H^{-1} \sum_{l=1}^{3} \left\langle \widehat{\delta b}\,,\, \overline{\Phi(n,l;\ .\ )} \right\rangle_{\hat{F}} \mathbf{e}_l \tag{43}$$

$$= \gamma_H^{-1} \sum_{l=1}^{3}\sum_{k=1}^{3} \hat{\alpha}_k \left\langle \widehat{\delta b}\,,\, \overline{S_k(n,l;\ .\ )} \right\rangle_{\hat{F}} \mathbf{e}_l .$$

Backprojection step:

$$\left(R^{'}[b]^*\zeta\right)(\mathbf{y}) = \gamma_b^{-1} \left\langle \hat{\zeta}\,,\, \Phi(\ .\ ,\ .\ ;\mathbf{y}) \right\rangle_{\hat{Z}} \tag{44}$$

$$= \gamma_b^{-1} \sum_{k=1}^{3} \hat{\alpha}_k \left\langle \hat{\zeta}\,,\, S_k(\ .\ ,\ .\ ;\mathbf{y}) \right\rangle_{\hat{Z}} .$$

7 A single step adjoint field inversion scheme

In this section we will describe briefly an extension of the single step adjoint field inversion scheme, which was introduced in [22] for the investigation of isotropic media, to the case of anisotropic media. It was already mentioned earlier that the method can be considered as a nonlinear generalization of the algebraic reconstruction technique (ART) in x-ray tomography [33], and it is also similar to the simultaneous iterative reconstruction technique (SIRT) as presented in [20] or to the Kaczmarz method for solving linear systems of equations (see also [33, 36]).

When solving the inverse problem which was formulated in section 2, we ideally want to find a parameter $\tilde{b}$ such that $R_j(\tilde{b}) = 0$ is satisfied for all given source positions $\mathbf{q}_j$, $j = 1, \dots, p$. In a Kaczmarz-type approach, we consider only one source at a time. Given a guess b for the parameters, and employing a Newton-type approach, we want to find a correction δb_j from the data corresponding to this source position such that

$$R_j^{'}[b]\delta b_j = -R_j(b). \tag{45}$$

We assume that (45) is underdetermined due to the limited amount of data which is used in this step. Therefore, equation (45) has many solutions (for a given residual $R_j(b) \in Z$), and we have to pick one according to some regularization criterion. We choose to take the solution which has minimal energy norm. This generalized solution of (45) has the explicit representation

$$\delta b_j = -R_j{'}[b]^* \left(R_j{'}[b] R_j{'}[b]^*\right)^{-1} R_j(b). \tag{46}$$

Some additional regularization can be incorporated in (46) as well, but we neglect these details of the reconstruction scheme in the following discussion. We use expression (46) to calculate our update δb_j from the residuals $R_j(b)$. The operator $C = \left(R_j{'}[b] R_j{'}[b]^*\right)^{-1}$ in (46) maps from Z into Z, and can be considered as a filtering operator acting on vectors in the data space. This operator is typically difficult to calculate in large scale inversion problems. Therefore, it might be advantageous to replace it by some easier to calculate nearby operator. Our experience from the numerical experiments performed in [22] shows that already the use of the identity (or some multiple of it) combined with a careful selection of source-receiver configurations is a good candidate for this operator. Similar strategies are reported in [21, 24, 34, 36] where a variety of inverse problems is considered. For the purpose of the present paper, it is sufficient to assume that we know C or some reasonable approximation to it.

With this approximation, all what is left to be done in order to calculate the correction δb_j to our best guess b is to apply the adjoint linearized residual operator $R_j'[b]^*$ to the (filtered) residuals $\zeta = CR_j(b)$. As we have shown in Theorem 4.1, this can be done very efficiently by just solving one forward Maxwell problem (15) in order to calculate $R_j(b)$ and $\mathbf{E}(\mathbf{x})$, and one adjoint Maxwell problem (18) in order to calculate $\mathcal{E}(\mathbf{x})$. Formula (20) yields then directly our correction δb_j.

In our single step (Kaczmarz type) adjoint field inversion scheme, we calculate this correction δb_j by using only the data corresponding to one single source $\mathbf{q}_j$. We premultiply this calculated correction δb_j with some (typically small) relaxation parameter κ, and then immediately apply it to the parameter b, which gives us a corrected parameter distribution $\check{b} = b + \kappa\delta b_j$. Then, when we use the set of data corresponding to the next source position $\mathbf{q}_{j+1}$ for calculating a new correction to $\check{b}$, we do this by running one forward and one adjoint Maxwell problem on the already corrected parameter distribution $\check{b}$.

As indicated in the discussion above, each of these single steps can be interpreted as an efficient numerical method for 'backprojecting' all (filtered) residuals corresponding to one source position *simultaneously* into the parameter space by solving just one adjoint Maxwell problem on the computer. The 'backprojection' automatically takes place along those sensitivity functions which correspond to the most recent best guess. Therefore, this inversion scheme is a *nonlinear* inversion method.

For more details about this single step inversion scheme, we again refer to the earlier publication [22]. A similar scheme has been applied in ultrasound tomography by Natterer and Wübbeling [34, 36], in more general bilinear inverse problems by Natterer [35], and in optical tomography by Dorn [21]. For alternative approaches to solving the inverse problem in 3D EMIT see for example [1, 2, 26, 27, 37] and the references given there.

8 Numerical examples for electromagnetic sensitivity functions

8.1 The Lost Hills model and its discretization

The numerical examples for sensitivity functions which we have calculated are based on the Lost Hills model which is described by Buettner [15]. The physical experiments of [15] have been done at Mobil Oil's Lost Hills-3 field in San Joaquin Valley, which is an interesting test site for our purposes since it can be viewed as an excellent analog of a shallow environmental remediation using steam injection. Earlier work at this test site has been done by Wilt *et al.* [48]. More information about the Lost Hills model can be found for example in [15].

The Lost Hills model in our numerical experiments consists of a layered background medium in which one or two 3D-inclusions are imbedded. There are six layers in total, of which the uppermost contains the air, and the remaining five layers contain soil and rock materials. The total size of the domain is (in XYZ-direction) $140 \times 210 \times 192.5$ m^3. The layers have, starting with the air and going downwards, extensions in Z-direction (in short 'Z-extension') of, respectively, 35 m (air, 0.0 Siemens/m), 35 m (soil, 0.3 S/m), 35 m (soil, 0.15 S/m), 17.5 m (soil, 0.06 S/m, contains inclusions), 35 m (soil, 0.06 S/m), and 35 m (soil, 0.2 S/m), where the numbers in parentheses give the conductivity values inside these layers. Inclusions (for example injected plumes of conducting steam) are located in the layer with a depth ranging from 70 m to 87.5 m below the free surface. The Z-extension of these plumes are, for simplicity, chosen to be the same as the Z-extension of the layer in which they are imbedded (17.5 m). It is assumed that the injected steam has a conductivity of 0.5 S/m in order to have a reasonable contrast to the background values (0.06 S/m). The relative permittivity and relative permeability are chosen to be 1.0 everywhere in all of our numerical examples. For more details see Figure 5.

We discretize the Lost Hills model described above by using a $40 \times 60 \times 55$ staggered grid for the physical domain, which is surrounded by 10 additional cells of PML (perfectly matched layer) on each side. The total grid (including PML) which is used in our computations is therefore $60 \times 80 \times 75$ grid cells. Each of the individual grid cells in the physical domain has a size of $3.5 \times 3.5 \times 3.5$ m^3, whereas those in the PML have a size of 10 m in the direction perpendicular to the boundary, and 3.5 m in the remaining directions. The total interior domain which is modelled by the computational grid without the PML has therefore the physical size $140 \times 210 \times 192.5$ m^3, and including the PML it has the physical size $340 \times 410 \times 392.5$ m^3.

The sources and adjoint sources (receivers) are in all examples x, y, or z-directed magnetic dipole sources of the strength 1 Am^2 and with frequency $f = 1.0$ kHz. They are located in two boreholes which are a distance of 30 grid cells or 105 m apart from each other, see Figure 5. We use two different depths for the source and receiver locations, one being at about 80 metres, and the other one at about 7 metres below the free surface. They are indicated in Figure 5 by the symbols 'F' ('Forward' sources) and 'A' ('Adjoint' sources or receivers). We use the Bi-CGSTAB scheme of van der Vorst [44] for the solution of the discretized Maxwell system. More specifically, we perform 700 iterations of the Bi-CGSTAB scheme for each forward and each adjoint problem. This yields typically a tolerance in the solution of about 5×10^{-7}. In our numerical experiments the Bi-CGSTAB scheme performs stably for the level of accuracy imposed. All calculations are performed on an SGI Octane.

8.2 Numerical experiments

The Figures 3–11 show the results of our numerical experiments. First, in order to make sure that our numerical forward modeling code works reliably, we have calculated analytical versions of the sensitivity functions for an infinitely extended homogeneous medium. The analytical formulas which are used for this calculation are derived in the appendix. The conductivity σ in the medium is 0.1 S/m everywhere, and the relative permittivity ϵ_r, as well as the relative permeability μ_r, are 1.0. The source is a z-directed magnetic dipole transmitter which is positioned in one borehole at a depth of 80 metres below the free surface, and the receiver is positioned in the other borehole at a depth of 7 metres below the free surface, and measures the z-component of the magnetic field. The frequency is, as in all of our numerical experiments, $f = 1$ KHz. Displayed in Figure 3 is the analytically calculated sensitivity function $S_z^{(x)}(1, z; \mathbf{y})$, where the lower index z indicates the orientation of the dipole source, the upper index x tells us that the sensitivity function with respect to a perturbation in the x-component of the anisotropic conductivity distribution is displayed, the arguments $(1, z)$ say that we are only looking at one single receiver position which measures the z-component of the magnetic field, and $\mathbf{y}$ is the independent variable of the sensitivity function ranging over all possible scattering positions in the medium.

We mention that all sensitivity functions in this paper are displayed on a logarithmic scale in the following sense. Let us define the values $\mathrm{Rmax}(k, i, l)$ and $\mathrm{Imax}(k, i, l)$ according to

$$\begin{aligned}
\mathrm{Rmax}(k,i,l) &= \max_{\mathbf{y}\in\Omega}\left\{\left|\mathrm{Re}(S_k^{(i)}(1,l;\mathbf{y}))\right|\right\}, \\
\mathrm{Imax}(k,i,l) &= \max_{\mathbf{y}\in\Omega}\left\{\left|\mathrm{Im}(S_k^{(i)}(1,l;\mathbf{y}))\right|\right\},
\end{aligned}$$

for $i, l, k \in \{x, y, z\}$. Here, the maximum is only taken over the finite number of computer evaluations of $S_k^{(i)}(1, l; \mathbf{y})$ which is given by the FDFD forward modelling code. This has the effect that all values of $S_k^{(i)}(1, l; \mathbf{y}))$ which contribute to Rmax and Imax are actually finite, whereas the theoretically calculated values would become singular at the source and receiver positions. With these reference values Rmax and Imax, we define the logarithmic sensitivity functions by

$$\begin{aligned}
\mathrm{logreal}(k,i,l;\mathbf{y}) &= \mathrm{sign}(\mathrm{Re}(S_k^{(i)}(1,l;\mathbf{y})))\left(60 - 10\times\log\left(\frac{\mathrm{Rmax}(k,i,l)}{|\mathrm{Re}(S_k^{(i)}(1,l;\mathbf{y}))|}\right)\right)_+ \\
\mathrm{logimag}(k,i,l;\mathbf{y}) &= \mathrm{sign}(\mathrm{Im}(S_k^{(i)}(1,l;\mathbf{y})))\left(60 - 10\times\log\left(\frac{\mathrm{Imax}(k,i,l)}{|\mathrm{Im}(S_k^{(i)}(1,l;\mathbf{y}))|}\right)\right)_+ .
\end{aligned}$$

Here, $\mathrm{sign}(x)$ gives the sign ('plus' or 'minus') of the real number x, the symbol $(x)_+ = \max\{0, x\}$ acts as the identity for positive values of x and delivers zero for negative values. 'Re' means 'real part', and 'Im' means 'imaginary part'. It is these logarithmic sensitivity functions which are displayed in the Figures 3–11. In all

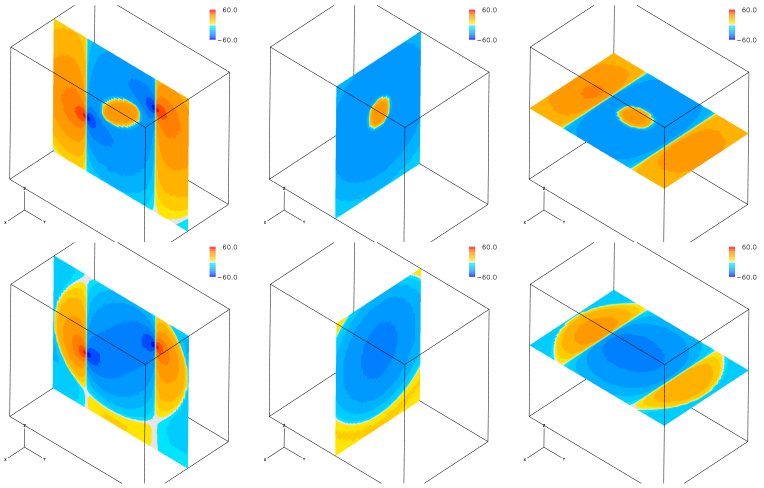

Figure 3: Shown is the analytically calculated x-component sensitivity function $S_z^{(x)}(1, z; \mathbf{y})$ as a function of $\mathbf{y}$ for an infinitely extended homogeneous medium. Source: z-directed dipole at depth 80 m. Receiver: z-directed dipole at depth 7 m. The scaling factors Rmax and Imax are chosen to be the same as in Figure 4 (FDFD calculation). Top row: real part logreal$(z, x, z; \mathbf{y})$. Bottom row: imaginary part logimag$(z, x, z; \mathbf{y})$. The functions logreal and logimag are defined in the text.

images which display analytically calculated sensitivity functions, we also use those reference values Rmax and Imax which have been calculated by using the FDFD forward modelling code for the given situation. That makes it easier to compare the analytically obtained functions and the numerically calculated functions with each other. The top rows of the figures always show logreal$(k, i, l; \mathbf{y})$ for one specific parameter combination (k, i, l), whereas the bottom rows show logimag$(k, i, l; \mathbf{y})$ for the same parameter combination.

The color scheme which we use in the figures is as follows. The values which logreal$(k, i, l; \mathbf{y})$ and logimag$(k, i, l; \mathbf{y})$ can assume range from -60 to 60. This range is divided equidistantly in the figures into 15 intervals. The first seven intervals contain only negative values, and are colored from dark blue (corresponding to values between -60 and -52) to light blue (corresponding to values between -12 and -4). The values close to zero (between -4 and 4) are displayed in white. Then, the positive values start with yellow areas (between 4 and 12) and go up to intense red areas (between 52 and 60).

In the following, we will give a short overview of the figures which are presented, and in section 9 we will discuss these figures in more details.

The top row of Figure 3 shows three different cross-sections of the real part of the analytically calculated sensitivity function $S_z^{(x)}(1, z; \mathbf{y})$, and the bottom row shows the same cross-sections but of the imaginary part. Clearly visible are the two

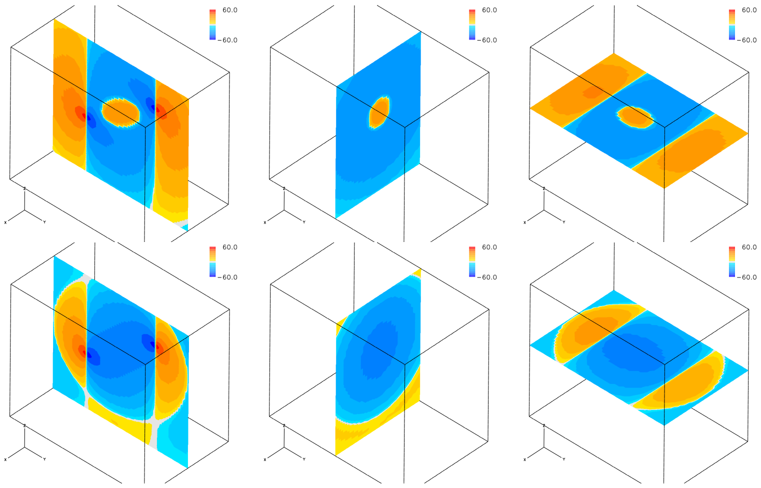

Figure 4: Shown is the numerically calculated x-component sensitivity function $S_z^{(x)}(1, z; \mathbf{y})$ as a function of $\mathbf{y}$ for an infinitely extended homogeneous medium. Source: z-directed dipole at depth 80 m. Receiver: z-directed dipole at depth 7 m. Scaling: Rmax $= 3.98 \times 10^{-13}$, Imax $= 1.22 \times 10^{-12}$. Top row: real part logreal$(z, x, z; \mathbf{y})$. Bottom row: imaginary part logimag$(z, x, z; \mathbf{y})$.

vertical planes across which the sensitivity function changes sign, as it is predicted by the analytical formula. These planes are defined by constant y-coordinates, one of them containing the source position, and the other one the receiver position. Figure 4 displays the same situation and the same cross sections as Figure 3, but now calculated by using the FDFD forward modelling code. These two figures show a very good agreement between the analytically calculated and the numerically calculated sensitivity functions, and indicate that our numerical code works reliably and can be used for calculating sensitivity functions in more complex situations.

Figure 5 shows the geometry of the Lost Hills example which we use for our numerical experiments in this paper. The left column of the figure shows the infinitely extended layered medium without any inclusions. In the middle column, we have imbedded in this layered medium a single inclusion of a moderately high contrast to the background conductivity distribution. The column on the right hand side of the figure shows a similar situation where two inclusions are now imbedded in the background layered medium.

Figure 6 shows the same sensitivity function and the same cross-sections as Figures 3 and 4, but now calculated for this layered medium. When comparing these three figures with each other, the most clearly visible difference between them is that the central 'orange' (i.e. 'positive') region in the real parts of the homogenous sensitivity functions has disappeared in the case of the layered medium. We will mention possible implications of this phenomenon for the reconstruction algorithm

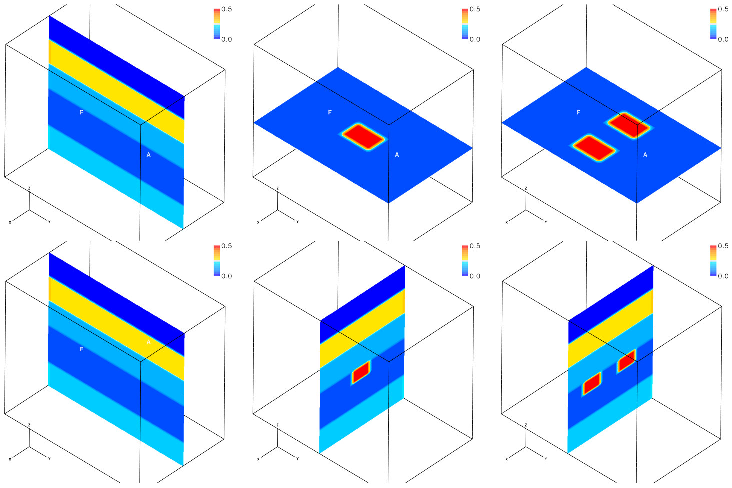

Figure 5: The figure shows the layered structure of the conductivity distribution in the Lost Hills model which is used in our numerical experiments. Left column: no inclusion. The symbol 'F' indicates source position, the symbol 'A' two possible receiver positions (one at the same depth as the source, the other one close to the free surface). Middle column: only one inclusion (plume). Right column: two inclusions.

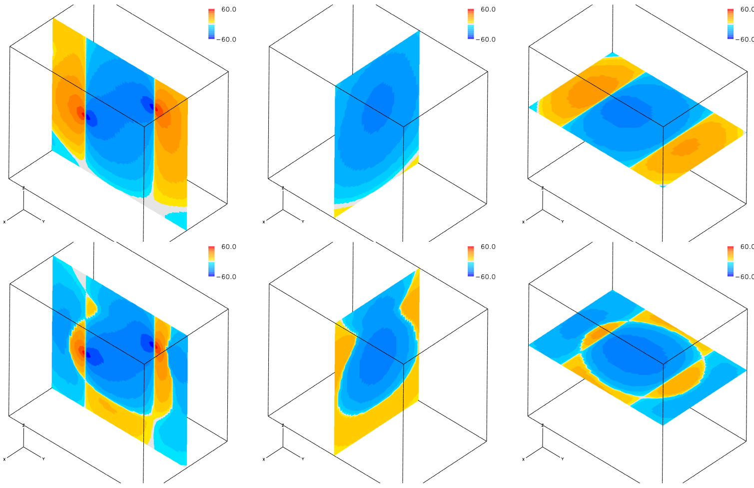

Figure 6: Shown is the numerically calculated x-component sensitivity function $S_z^{(x)}(1, z; \mathbf{y})$ as a function of $\mathbf{y}$ for an infinitely extended layered medium. Source: z-directed dipole at depth 80 m. Receiver: z-directed dipole at depth 7 m. Scaling: Rmax $= 7.19 \times 10^{-13}$, Imax $= 5.18 \times 10^{-13}$. Top row: real part logreal$(z, x, z; \mathbf{y})$. Bottom row: imaginary part logimag$(z, x, z; \mathbf{y})$.

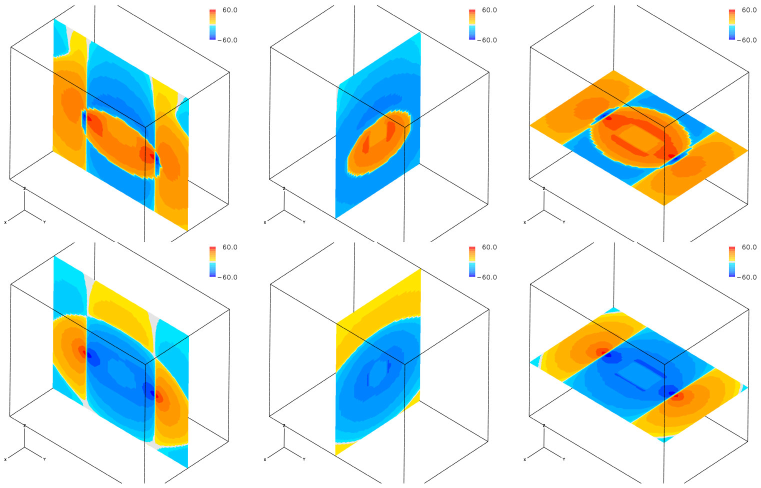

Figure 7: Shown is the numerically calculated x-component sensitivity function $S_z^{(x)}(1,z;\mathbf{y})$ as a function of $\mathbf{y}$ for an infinitely extended layered medium with one inclusion. Source: z-directed dipole at depth 80 m. Receiver: z-directed dipole at depth 80 m. Scaling: Rmax $= 3.43 \times 10^{-13}$, Imax $= 2.28 \times 10^{-12}$. Top row: real part logreal$(z,x,z;\mathbf{y})$. Bottom row: imaginary part logimag$(z,x,z;\mathbf{y})$.

in the following section when discussing the results of our numerical experiments in more details.

In the Figures 7 and 8, we investigate the influence of some embedded inclusions on the shapes of the sensitivity functions. In particular, we are interested in the question whether certain combinations of inclusions might have a 'channeling effect' on the probing fields which will focus the sensitivities of the data to certain regions in the medium and makes it more difficult to resolve features in the reconstructions which are outside of these focussed regions. This effect makes the inverse problem highly nonlinear and ill-posed. The two figures display the same cross-sections, such that we can easily compare them with each other.

Figure 7 shows the situation where one single object of high contrast is embedded in the layered medium. The source and the receiver are positioned at approximately the same depth as the inclusion. We see that the sensitivities try to 'avoid' this inclusion in the sense that the absolute values of the sensitivities inside these objects are much smaller than in the regions immediately surrounding the inclusion. A similar phenomenon is observed in Figure 8 where two high contrast inclusions are present at approximately the same depth as the source and the receiver. The sensitivities seem to be 'channeled' between these two inclusions, concentrating in the regions between the objects, and having reduced values inside the two inclusions.

Notice that in the figures described so far we always have displayed the x-component sensitivity functions of the given situations. The main reason for this

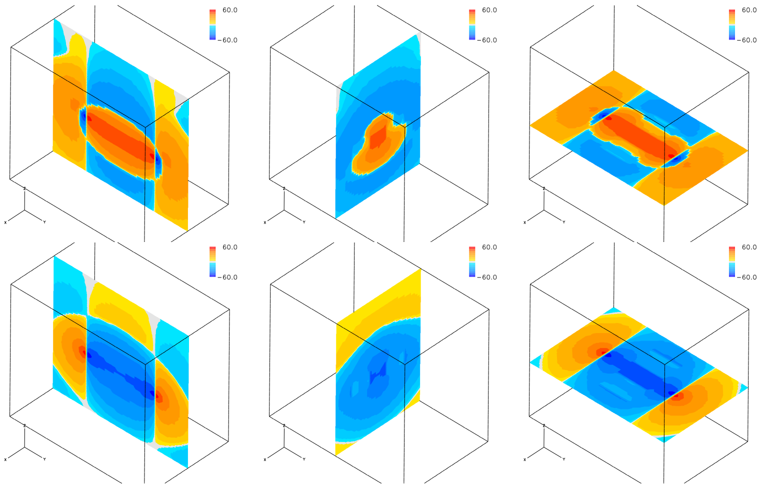

Figure 8: Shown is the numerically calculated x-component sensitivity function $S_z^{(x)}(1, z; \mathbf{y})$ as a function of $\mathbf{y}$ for an infinitely extended layered medium with two inclusions. Source: z-directed dipole at depth 80 m. Receiver: z-directed dipole at depth 80 m. Scaling: Rmax $= 7.26 \times 10^{-13}$, Imax $= 2.73 \times 10^{-12}$. Top row: real part logreal$(z, x, z; \mathbf{y})$. Bottom row: imaginary part logimag$(z, x, z; \mathbf{y})$.

is our observation that this component is the dominant component in most of our numerically calculated sensitivities. This behavior is also indicated by the theoretical expressions for the sensitivity functions in the homogeneous case (see the appendix). Therefore, we will not address the other cases of y- and z-component sensitivity functions explicitly in this paper, although we believe that they certainly have to be taken into account when designing inversion algorithms for general background media. Instead, we will show one example where we compare the x-component sensitivity function with the isotropic sensitivity function, the latter one being essentially the sum of the corresponding x-, y-, and z-component sensitivity functions. Moreover, so far we only have considered the situation where the given receiver measures the z-component of the magnetic field. The question remains how do the sensitivity functions look like for receivers measuring different components of the magnetic field.

The following three figures have been selected in order to address some of the above mentioned questions. All three figures show a situation where the receiver measures the y-component of the magnetic field, and where the source is as above a z-directed dipole transmitter. Both, the source and the receiver, are located at the same depth, namely 80 m below the free surface. The three figures display the same cross-sections, such that we can easily compare them with each other.

Figure 9 shows the x-component sensitivity function in this situation for an infinitely extended *homogeneous* medium. Compare the corresponding analytical

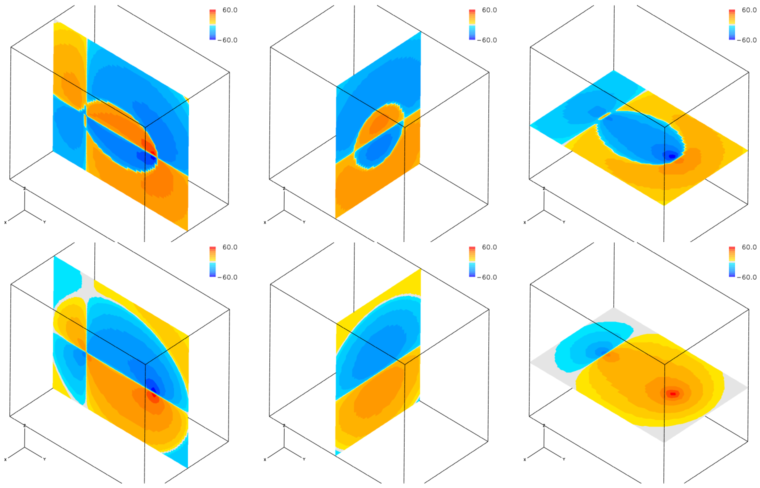

Figure 9: Shown is the numerically calculated x-component sensitivity function $S_z^{(x)}(1, y; \mathbf{y})$ as a function of $\mathbf{y}$ for an infinitely extended homogeneous medium. Source: z-directed dipole at depth 80 m. Receiver: y-directed dipole at depth 80 m. Scaling: Rmax $= 3.36 \times 10^{-13}$, Imax $= 2.96 \times 10^{-12}$. Top row: real part logreal$(z, x, y; \mathbf{y})$. Bottom row: imaginary part logimag$(z, x, y; \mathbf{y})$.

formula which is given in the appendix. It correctly predicts the two orthogonal planes in the figure where the sensitivity function changes sign: a vertical plane of constant y-coordinate containing the source position, and a horizontal plane of constant z-coordinate containing the receiver position. Figure 10 shows again the x-component sensitivity function for the same situation, but in an infinitely extended *layered* medium. Finally, Figure 11 shows the *isotropic* sensitivity function for the case of an infinitely extended layered medium. Notice that the x-component sensitivity in Figure 10 and the isotropic sensitivity in Figure 11 look very similar, which is due to the fact that the y- and z-component sensitivities are of much smaller magnitude than the x-component sensitivity. However, certain differences between these two figures are also clearly visible, which means that the y- and z-component sensitivities are not completely zero as in the homogeneous case. Comparison of Figures 10 and 11 with Figure 9, on the other hand, shows that the layering of the background medium has also here a significant influence on the shapes of the sensitivity functions.

Similar effects as shown above can also be observed in the other examples for sensitivity functions which we have calculated so far with our FDFD forward modeling code. However, we will restrict ourselves in this paper to the discussion of the figures which we have described above. In the next section, we will provide a more in-depth discussion of the presented figures, and will point out some possible consequences for our adjoint field inversion algorithm when used for the imaging of

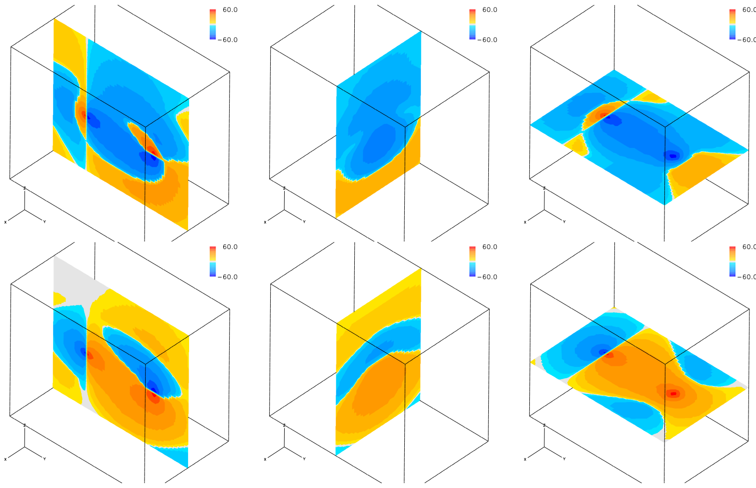

Figure 10: Shown is the numerically calculated x-component sensitivity function $S_z^{(x)}(1, y; \mathbf{y})$ as a function of $\mathbf{y}$ for an infinitely extended layered medium. Source: z-directed dipole at depth 80 m. Receiver: y-directed dipole at depth 80 m. Scaling: Rmax $= 8.27 \times 10^{-13}$, Imax $= 2.54 \times 10^{-12}$. Top row: real part logreal$(z, x, y; \mathbf{y})$. Bottom row: imaginary part logimag$(z, x, y; \mathbf{y})$.

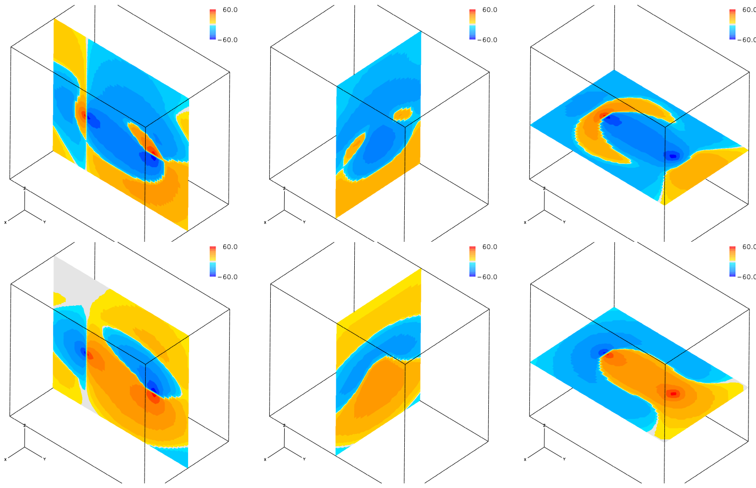

Figure 11: Shown is the numerically calculated isotropic sensitivity function $S_z^{(0)}(1, y; \mathbf{y})$ as a function of $\mathbf{y}$ for an infinitely extended layered medium. Source: z-directed dipole at depth 80 m. Receiver: y-directed dipole at depth 80 m. Scaling: Rmax $= 8.27 \times 10^{-13}$, Imax $= 2.54 \times 10^{-12}$. Top row: real part logreal$(z, iso, y; \mathbf{y})$. Bottom row: imaginary part logimag$(z, iso, y; \mathbf{y})$.

isotropic as well as anisotropic media given 3D electromagnetic data.

9 Discussion

We have presented in section 8 the results of our numerical experiments for four different situations. The first one considered an infinitely extended homogeneous background medium, the second one an infinitely extended layered medium, and the third and fourth ones an infinitely extended layered medium with one or two inclusions, respectively. In the application which we have in mind, namely the imaging of pollutant plumes in the earth from cross-borehole electromagnetic data, we assume that the layered medium situation is more realistic than the homogeneous background assumption. Moreover, since the inclusions which we are looking for in the inversion task, have a moderate to high contrast to the background conductivity distribution, we assume that the imaging problem is highly nonlinear and ill-posed, and straightforward linearization methods like the Born approximation might not be justified. In this section we investigate some possible implications of these assumptions for the imaging process from the point of view of sensitivity analysis. We will also address the role of anisotropy in the reconstruction process.

First, we compare Figures 4 and 6. The experimental setup is the same in both figures, but Figure 4 is calculated with the assumption of a homogeneous medium, and Figure 6 with the assumption of a layered medium. A clearly visible difference between these two results is the oval area in the real part just halfway between source and receiver which has a changed sign in the case of a homogeneous medium (it is colored orange there) but not in the case of a layered medium. Assuming that the physically given medium is layered, any parameter perturbation inside this oval area will affect the data at the given receiver with a negative sign. However, if the reconstruction is done with the assumption of a homogeneous medium (as for example in the simplest form of the Born approximation) then the correction of the parameter in the backprojection step will be done according to the 'incorrect' positive sign as it is given in the sensitivity function of the homogenous medium. Therefore, instead of reducing the misfit in the parameter values, it will increase it in this area. This can have the effect of destabilizing the inversion routine, unless the updates corresponding to different source-receiver pairs are able to compensate for this discrepancy.

A similar situation is observed in Figures 9 and 10. They again show the same experimental setup, but Figure 9 uses the assumption of a homogeneous medium, whereas Figure 10 uses the assumption of a layered background medium. Although the general forms of these two sensitivity functions are very similar, the areas where the signs change from positive to negative are shifted. This has again the effect that a parameter perturbation in a layered medium which affects the data with a certain sign, can give rise to a correction of this parameter at the given position with an incorrect sign if calculated with the homogeneous sensitivity functions. This tends to destabilize the inversion process.

Next, we investigate the influence of high contrast inclusions on the reconstruction process. Figure 7 shows a situation with only one high contrast inclusion, and Figure 8 shows the same situation but with two high contrast inclusions. Both figures show that the sensitivities tend to concentrate outside the inclusions, and that they have smaller values inside them. We expect that this 'channeling effect' will become even more visible if the contrast is further increased. The channeling phenomenon makes the inverse problem highly nonlinear. The sensitivity functions corresponding to a more uniform (for example layered) background parameter distribution look quite different from the sensitivity functions of the high contrast situation which show this channeling effect. If the inversion process is started with for example the layered background parameter distribution, the first task of the reconstruction algorithm is to recover the basic structure of the high contrast inclusions. However, we expect that it becomes more and more difficult for later updates to recover information inside these high contrast inclusions since, as these inclusions build up in the reconstructions, the sensitivity functions will more and more be channeled around the inclusions such that the data become less sensitive to details of the structures inside the inclusions. We mention that a more theoretical study of a similar channeling effect in the situation of impedance tomography, and an alternative approach for solving the inversion problem, can be found in Borcea *et al* [13, 14].

We want to concentrate next on the influence of anisotropy on the reconstruction process. We mentioned already earlier that many source-receiver combinations are very sensitive to certain components of the anisotropic parameters, and much less sensitive to other components. This phenomenon is especially visible in the situation of a homogeneous background medium, which follows directly from the analytical forms of the sensitivity functions as they are derived in the appendix. But also in the case of a layered medium this phenomenon can be observed. See for example Figures 10 and 11 which show the x-component sensitivity function and the isotropic sensitivity function for the given situation. Since the isotropic sensitivity function is essentially the sum of the x, y and z-component sensitivity functions, the similarity of these two figures indicates that the y- and z-component sensitivities are much smaller in magnitude than the x-component sensitivity. This is also verified by the analytical formula for this situation in the case of a homogeneous background medium. If we want to image all three components of the parameter distribution with the same accuracy, we will therefore need a sufficiently rich variety of different source-receiver combinations for gathering the data.

Similar observations hold true for the spatial dependence of the sensitivities which are used for the inversion. From the interpretation of the individual steps of the reconstruction algorithm as backprojection steps, it follows that those positions where all sensitivities are small are difficult to recover and might give rise to artifacts in the reconstructions. The backprojected residuals which are due to these parameter perturbations will tend to concentrate on different areas of the imaging domain. We mention that iterative schemes are typically more likely to be able to correct for these errors of early updates. One-step inversion methods, as for example the Born approximation, typically cannot correct for these errors.

There are many more features of the sensitivity functions which are interesting to investigate. We will restrict ourselves in the following to mentioning a few topics where we believe the study of sensitivity relations (as it was done above) can provide valuable information about optimal ways of gathering and interpreting electromagnetic data for geophysical applications. These topics also indicate some possible directions for future research.

First, when imaging a geophysical test site, some decision has to be made about what degree of anisotropy should be expected in the given situation. For a discussion of some implications of electrical anisotropy in applications see also Weidelt [47]. We noticed already that the shapes of the x, y and z-component sensitivity functions typically differ from each other, and certain source-receiver configurations are very sensitive to some of these components and much less sensitive to others. This indicates that it should in general be possible to resolve anisotropic structures in the earth from electromagnetic data, provided that a sufficient amount of appropriately gathered data is available. On the other hand, it indicates that the treatment of strongly anisotropic media with an isotropic imaging approach can lead to inaccurate reconstructions because of the related misinterpretations of the data.

Second, in basically all imaging problems the question comes up what degree of resolution can be expected from the reconstructions. In our situation, since the reconstructions are essentially results of a series of backprojection steps, only features of the medium can be recovered which are actually represented by the sensitivity functions. This gives us some information about the resolution which we can expect. If we want to further quantify the degree of resolution, we could use for example the concept of a 'resolution matrix' which has been discussed in the similar situation of hydrology by Vasco *et al* [45]. Also see [11, 12] for a discussion of efficient computational means of estimating the resolution matrix. The sensitivity functions play a natural role in this approach, which is not very surprising since we would intuitively expect that for example the broadening of the sensitivity functions some distance away from the sources and receivers will give rise to a decrease in the resolution of our imaging method at these points. A similar observation was already mentioned above in the discussion of the broadening of the sensitivity functions in optical tomography which leads to a decreased resolution compared to x-ray tomography. See for example [4, 5, 6, 23].

Third, the knowledge of the general form of the sensitivity functions can be used in order to design experiments more efficiently. See for example Maurer *et al* [30] and the references therein for a discussion of possible design strategies for electromagnetic geophysical surveys. The Fréchet derivative plays an important role in these strategies, and we have seen above that the Fréchet derivative is directly related to our sensitivity functions. A possible design strategy would for example be to combine sources and receivers in a way such that the resulting sensitivity structure is focused on certain regions of interest in the earth and is small in other areas. This typically has to be done under certain constraints on the availability and number of boreholes, on the given source pattern and receiver characteristics, and other test site specific constraints. We refer for more details again to [30] and the references given there.

Appendix

A: Analytical forward sensitivity analysis for anisotropic media

In forward sensitivity analysis, we decompose the linearized residual operator into sensitivity functions by only using Green functions of the forward problem (27) but not of the adjoint problem (28). If the background medium is an infinitely extended homogeneous medium, then explicit expressions for these Green functions are available. Next, we will present a standard way of deriving sensitivity relations in this situation for the example of a z-directed magnetic dipole source at the location $\mathbf{x}_s$, and a single magnetic dipole receiver at the location $\mathbf{x}_d$ which can be x-, y-, or z-directed. We will denote the residual operator corresponding to a z-directed receiver in the following by $R_z^{'}[b]$, and the residual operators corresponding to x- and y-directed receivers by $R_x^{'}[b]$ and $R_y^{'}[b]$, respectively. We introduce the notation

$$\begin{aligned} k^2 &= \omega^2\mu\epsilon - i\omega\mu\sigma, \\ r_s^2 &= (x_{sc}-x_s)^2 + (y_{sc}-y_s)^2 + (z_{sc}-z_s)^2, \\ r_d^2 &= (x_{sc}-x_d)^2 + (y_{sc}-y_d)^2 + (z_{sc}-z_d)^2, \end{aligned}$$

where the index s stands for 'source', the index d for 'detector', and the index sc for an arbitray scattering point in the domain.

Let $G_{he,z}(\mathbf{x}_s;\mathbf{x}_{sc})$, $G_{hh,z}(\mathbf{x}_s;\mathbf{x}_{sc})$ be the solution of the problem

$$\Lambda_M(b)\begin{pmatrix} G_{he,z} \\ G_{hh,z} \end{pmatrix} = \begin{pmatrix} 0 \\ -i\omega\mu m_s\delta(\mathbf{x}-\mathbf{x}_s)\mathbf{e}_z \end{pmatrix} \tag{47}$$

evaluated at $\mathbf{x}_{sc}$. In (47), the field is calculated which is due to a z-directed harmonic magnetic dipole source. A small loop of current I at the point $\mathbf{x}_s = (x_s, y_s, z_s)$ parallel to the $x-y$ plane is represented by an infinitesimal magnetic dipole with moment $m_s = IdS$, where dS is the area of the loop. The magnetization vector is given by

$$\mathbf{m}(\mathbf{x}) = m_s\delta(x-x_s)\delta(y-y_s)\delta(z-z_s)\mathbf{e}_z.$$

We use the analytic formulas for $G_{he,z}(\mathbf{x}_s;\mathbf{x}_{sc})$, $G_{hh,z}(\mathbf{x}_s;\mathbf{x}_{sc})$ in the case of an infinitely extended homogeneous medium which are given in [46]. Some distance away from the magnetic dipole source we have

$$G_{he,z}(\mathbf{x}_s;\mathbf{x}_{sc}) = \frac{i\omega\mu m_s}{4\pi r_s^3}(ikr_s+1)e^{-ikr_s}\Big((y_{sc}-y_s)\mathbf{e}_x - (x_{sc}-x_s)\mathbf{e}_y\Big).$$

In a similar way, let $G_{ee,i}(\mathbf{x}_{sc};\mathbf{x})$, $G_{eh,i}(\mathbf{x}_{sc};\mathbf{x})$ for an arbitrary $\mathbf{x}_{sc}\in\Omega$ be the solutions of the problems

$$\Lambda_M(b)\begin{pmatrix} G_{ee,i} \\ G_{eh,i} \end{pmatrix} = \begin{pmatrix} m_e\delta(\mathbf{x}-\mathbf{x}_{sc})\mathbf{e}_i \\ 0 \end{pmatrix}, \quad i\in x,y,z. \tag{48}$$

In (48), the field is calculated which is due to a harmonic electric dipole source, where $i \in \{x, y, z\}$ indicates the orientation of the dipole. The corresponding source term with $m_e = Ids$ is

$$\mathbf{J}(\mathbf{x}) \;=\; m_e \delta(x - x_{sc})\delta(y - y_{sc})\delta(z - z_{sc})\mathbf{e}_i,$$

which describes a line element of infinitesimal length ds and with current density I located at the point $\mathbf{x}_{sc} = (x_{sc}, y_{sc}, z_{sc}) \in \Omega$. The analytical expressions for the functions $G_{eh,x}(\mathbf{x}_{sc}; \mathbf{x}_d)$, $G_{eh,y}(\mathbf{x}_{sc}; \mathbf{x}_d)$ some distance away from the (scattering-) sources are [46]

$$\begin{aligned} G_{eh,x}(\mathbf{x}_{sc}; \mathbf{x}_d) &= \frac{m_e}{4\pi r_d^3}(ikr_d + 1)e^{-ikr_d}\Big(- (z_d - z_{sc})\mathbf{e}_y \;+\; (y_d - y_{sc})\mathbf{e}_z\Big), \\ G_{eh,y}(\mathbf{x}_{sc}; \mathbf{x}_d) &= \frac{m_e}{4\pi r_d^3}(ikr_d + 1)e^{-ikr_d}\Big(- (x_d - x_{sc})\mathbf{e}_z \;+\; (z_d - z_{sc})\mathbf{e}_x\Big). \end{aligned}$$

From (16), (17) we get for a z-directed source and an l-directed receiver, $l \in \{x, y, z\}$, the expression

$$R_l'[b]\,\delta b \;=\; \sum_{i=1}^{3} \int_\Omega G_{he,z}^{(i)}(\mathbf{x}_s; \mathbf{x}_{sc})\delta b^{(i)}(\mathbf{x}_{sc}) G_{eh,i}^{(l)}(\mathbf{x}_{sc}; \mathbf{x}_d)\, d\mathbf{x}_{sc}. \tag{49}$$

We define the *direct forms of the anisotropic sensitivity functions* $S_l^{(i)}(\mathbf{x}_{sc})$ by

$$S_l^{(i)}(\mathbf{x}_{sc}) \;=\; G_{he,z}^{(i)}(\mathbf{x}_s; \mathbf{x}_{sc}) G_{eh,i}^{(l)}(\mathbf{x}_{sc}; \mathbf{x}_d) \tag{50}$$

for $i, l \in \{x, y, z\}$. With these functions, equation (49) reads for an x-directed receiver

$$R_x'[b]\,\delta b \;=\; \sum_{i=1}^{3} \int_\Omega S_x^{(i)}(\mathbf{x}_{sc})\delta b^{(i)}(\mathbf{x}_{sc})\, d\mathbf{x}_{sc}$$

with

$$\begin{aligned} S_x^{(x)}(\mathbf{x}_{sc}) &= 0, \\ S_x^{(y)}(\mathbf{x}_{sc}) &= \beta_f\,(x_{sc} - x_s)(z_{sc} - z_d), \\ S_x^{(z)}(\mathbf{x}_{sc}) &= 0, \end{aligned}$$

and

$$\beta_f \;=\; \left(\frac{i\omega\mu m_s}{4\pi r_s^3}\right)\left(\frac{m_e}{4\pi r_d^3}\right)(ikr_s + 1)(ikr_d + 1)e^{-ikr_s}e^{-ikr_d}.$$

In the same way, we get for a y-directed receiver

$$R_y'[b]\,\delta b \;=\; \sum_{i=1}^{3} \int_\Omega S_y^{(i)}(\mathbf{x}_{sc})\delta b^{(i)}(\mathbf{x}_{sc})\, d\mathbf{x}_{sc}$$

with

$$\begin{aligned}
S_y^{(x)}(\mathbf{x}_{sc}) &= \beta_f\,(y_{sc}-y_s)(z_{sc}-z_d),\\
S_y^{(y)}(\mathbf{x}_{sc}) &= 0,\\
S_y^{(z)}(\mathbf{x}_{sc}) &= 0,
\end{aligned}$$

and for a z-directed receiver

$$R_z'[b]\,\delta b = \sum_{i=1}^{3}\int_\Omega S_z^{(i)}(\mathbf{x}_{sc})\delta b^{(i)}(\mathbf{x}_{sc})\,d\mathbf{x}_{sc}$$

with

$$\begin{aligned}
S_z^{(x)}(\mathbf{x}_{sc}) &= -\beta_f\,(y_{sc}-y_s)(y_{sc}-y_d),\\
S_z^{(y)}(\mathbf{x}_{sc}) &= -\beta_f\,(x_{sc}-x_s)(x_{sc}-x_d),\\
S_z^{(z)}(\mathbf{x}_{sc}) &= 0.
\end{aligned}$$

For an isotropic medium $b^{(0)} := b^{(1)} = b^{(2)} = b^{(3)}$ we get the following decompositions

$$R_l'[b^{(0)}]\,\delta b^{(0)} = \int_\Omega S_l^{(0)}(\mathbf{x}_{sc})\delta b^{(0)}(\mathbf{x}_{sc})\,d\mathbf{x}_{sc},$$

for $l \in \{x,y,z\}$, with the *direct forms of the isotropic sensitivity functions*

$$\begin{aligned}
S_x^{(0)}(\mathbf{x}_{sc}) &= \beta_f(x_{sc}-x_s)(z_{sc}-z_d)\\
S_y^{(0)}(\mathbf{x}_{sc}) &= \beta_f(y_{sc}-y_s)(z_{sc}-z_d)\\
S_z^{(0)}(\mathbf{x}_{sc}) &= -\beta_f\Big((y_{sc}-y_s)(y_{sc}-y_d)\;+\;(x_{sc}-x_s)(x_{sc}-x_d)\Big).
\end{aligned}$$

These expressions are similar to the expressions derived by Spies and Habashy [43].

B: Analytical adjoint sensitivity analysis for anisotropic media

In adjoint sensitivity analysis, we decompose the linearized residual operator into sensitivity functions by using Green functions for the forward problem (27) as well as for the adjoint problem (28). These forms are analogous to the forms in (29) and are given by

$$R_l'[b]\,\delta b = \sum_{i=1}^{3}\int_\Omega \tilde{S}_l^{(i)}(\mathbf{x}_{sc})\delta b^{(i)}(\mathbf{x}_{sc})\,d\mathbf{x}_{sc}$$

for $l \in \{x,y,z\}$ where $\tilde{S}_l^{(i)}(\mathbf{x}_{sc})$ are the *adjoint forms of the anisotropic sensitivity functions.*

Let $\Gamma_{he,l}(\mathbf{x}_d;\mathbf{x})$, $\Gamma_{hh,l}(\mathbf{x}_d;\mathbf{x})$ be the solutions of the adjoint problem

$$\begin{aligned}
\nabla\times\Gamma_{hh,l}\;-\;\overline{b(\mathbf{x})}\Gamma_{he,l} &= 0,\\
\nabla\times\Gamma_{he,l}\;+\;\overline{a(\mathbf{x})}\Gamma_{hh,l} &= m_m\delta(\mathbf{x}-\mathbf{x}_d)\mathbf{e}_l.
\end{aligned}$$

Then, $\phi = \overline{\Gamma_{he,l}}$ and $\psi = \overline{\Gamma_{hh,l}}$ solve

$$\begin{aligned}\nabla \times \psi \,-\, b(\mathbf{x})\phi &= 0,\\ \nabla \times \phi \,+\, a(\mathbf{x})\psi &= \overline{m}_m \delta(\mathbf{x}-\mathbf{x}_d)\mathbf{e}_l.\end{aligned}$$

Analytical forms for these solutions are given in Ward and Hohmann [46]. We will need

$$\begin{aligned}\overline{\Gamma}_{he,x}(\mathbf{x}_d;\mathbf{x}_{sc}) &= \frac{-\overline{m}_m}{4\pi r_d^3}(ikr_d+1)e^{-ikr_d}\Big((z_{sc}-z_d)\mathbf{e}_y \,-\, (y_{sc}-y_d)\mathbf{e}_z\Big),\\ \overline{\Gamma}_{he,y}(\mathbf{x}_d;\mathbf{x}_{sc}) &= \frac{-\overline{m}_m}{4\pi r_d^3}(ikr_d+1)e^{-ikr_d}\Big((x_{sc}-x_d)\mathbf{e}_z \,-\, (z_{sc}-z_d)\mathbf{e}_x\Big),\\ \overline{\Gamma}_{he,z}(\mathbf{x}_d;\mathbf{x}_{sc}) &= \frac{-\overline{m}_m}{4\pi r_d^3}(ikr_d+1)e^{-ikr_d}\Big((y_{sc}-y_d)\mathbf{e}_x \,-\, (x_{sc}-x_d)\mathbf{e}_y\Big).\end{aligned}$$

The adjoint anisotropic sensitivity functions, $\tilde{S}_l^{(i)}(\mathbf{x}_{sc})$, are now given by

$$\tilde{S}_l^{(i)}(\mathbf{x}_{sc}) \;=\; G_{he,z}^{(i)}(\mathbf{x}_s;\mathbf{x}_{sc})\overline{\Gamma}_{he,l}^{(i)}(\mathbf{x}_d;\mathbf{x}_{sc}) \tag{51}$$

for $i,l \in \{x,y,z\}$. We get

$$\begin{aligned}\tilde{S}_x^{(x)}(\mathbf{x}_{sc}) &= 0,\\ \tilde{S}_x^{(y)}(\mathbf{x}_{sc}) &= -\beta_a\,(x_{sc}-x_s)(z_{sc}-z_d),\\ \tilde{S}_x^{(z)}(\mathbf{x}_{sc}) &= 0,\end{aligned}$$

and

$$\begin{aligned}\tilde{S}_y^{(x)}(\mathbf{x}_{sc}) &= -\beta_a\,(y_{sc}-y_s)(z_{sc}-z_d),\\ \tilde{S}_y^{(y)}(\mathbf{x}_{sc}) &= 0,\\ \tilde{S}_y^{(z)}(\mathbf{x}_{sc}) &= 0,\end{aligned}$$

and

$$\begin{aligned}\tilde{S}_z^{(x)}(\mathbf{x}_{sc}) &= \beta_a\,(y_{sc}-y_s)(y_{sc}-y_d),\\ \tilde{S}_z^{(y)}(\mathbf{x}_{sc}) &= \beta_a\,(x_{sc}-x_s)(x_{sc}-x_d),\\ \tilde{S}_z^{(z)}(\mathbf{x}_{sc}) &= 0.\end{aligned}$$

Here,

$$\beta_a \;=\; \left(\frac{i\omega\mu m_s}{4\pi r_s^3}\right)\left(\frac{-\overline{m}_m}{4\pi r_d^3}\right)(ikr_s+1)(ikr_d+1)e^{-ikr_s}e^{-ikr_d}.$$

Putting $m_e = \overline{m_m} = 1$ (and adapting physical dimensions in (50), (51)) we get

$$\beta_a \;=\; -\left(\frac{i\omega\mu m_s}{4\pi r_s^3}\right)\left(\frac{1}{4\pi r_d^3}\right)(ikr_s+1)(ikr_d+1)e^{-ikr_s}e^{-ikr_d} \;=\; -\beta_f.$$

Therefore, we recover the same expressions as in the forward sensitivity analysis.

C: Discretization of Maxwell's equations

In this section we briefly describe the numerical forward solver which we use to model the 3D system of Maxwell's equations in an infinite or semi-infinite domain for anistropic media. A more detailed description of the algorithm can be found in [17, 18, 22].

The code we use is a finite-difference frequency domain (FDFD) code which was developed by Champagne *et al.* [17, 18] for modeling the propagation of electromagnetic radiation in conductive materials. The implementation given in [17, 18] can be considered as an extension to lossy and anisotropic media of a finite-difference frequency-domain formulation that was developed earlier by Beilenhoff *et al.* [9] for boundary scattering in lossless and isotropic media. Since we have to model an infinite medium using a finite-dimensional computational domain, we use in addition an anisotropic PML (perfectly matched layer) in order to avoid reflections at the artificial computational boundaries. Here the work of Berenger [10] and Sacks *et al.* [41] is followed. The absorbing regions are chosen to have material parameters similar to those proposed by Kuzuoglu *et al.* [29]. The code is designed to be able to model media with general anisotropic parameter distributions $b(\mathbf{x})$ and $a(\mathbf{x})$ in the domain Ω. Anisotropy is expected to become practically important, for example, when model cells contain oriented fractures filled with conducting fluid.

The derivation of the FDFD formulation starts from an integral representation of Maxwell's curl equations (Ampère's and Faraday's laws) (1),(2):

$$\oint_{\mathcal{C}} \mathbf{H} \cdot dl \;=\; i\omega \int_{\mathcal{S}} (\overline{\epsilon} \cdot \mathbf{E}) \cdot \mathbf{n} \, dS \;+\; \int_{\mathcal{S}} \mathbf{J} \cdot \mathbf{n} \, dS \tag{52}$$

and

$$\oint_{\mathcal{C}} \mathbf{E} \cdot dl \;=\; -i\omega \int_{\mathcal{S}} (\overline{\mu} \cdot \mathbf{H}) \cdot \mathbf{n} \, dS \;+\; \int_{\mathcal{S}} \mathbf{M} \cdot \mathbf{n} \, dS, \tag{53}$$

where $\mathcal{C}$ is the boundary of the open surface S, and $\mathbf{n}$ denotes the unit normal vector at a given point on this boundary. The parameters $\overline{\epsilon}$ and $\overline{\mu}$ (where the bars over the symbols indicate in this paragraph always a result of some averaging procedure rather than 'complex conjugate') are diagonal dyads with complex numbers on the main diagonal. They are related to the parameters a and b inside the domain Ω by

$$\overline{\mu}(\mathbf{x}) \;=\; (i\omega)^{-1}\overline{a}(\mathbf{x}), \qquad \overline{\epsilon}(\mathbf{x}) \;=\; (i\omega)^{-1}\overline{b}(\mathbf{x}),$$

where $\overline{a}(\mathbf{x})$ and $\overline{b}(\mathbf{x})$ are values of $a(\mathbf{x})$ and $b(\mathbf{x})$ averaged over a small neighborhood of the given point $\mathbf{x} \in \Omega$. In the surrounding PML material the three components of the diagonal dyads $\overline{a}(\mathbf{x})$ and $\overline{b}(\mathbf{x})$ at a given point are chosen carefully to achieve the desired properties of the absorbing PML region, namely being nonreflecting for radiation leaving the interior of the computational domain.

The computational domain is discretized into small boxes (elementary cells) using a staggered grid (see Figure 2). All material parameters are assumed constant in a given elementary cell. The electric field values and the values of the material parameter b are attached to the central points of the edges of these boxes, whereas

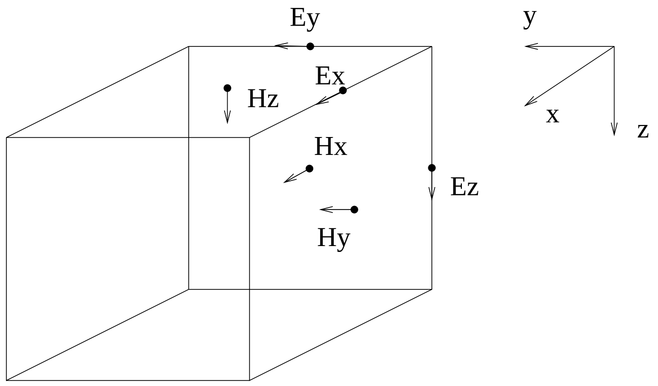

Figure 12: One box of the staggered grid. The electric field values and the values of the material parameter b are attached to the central points of the edges of these boxes, whereas all magnetic field values and the values of the material parameter a are attached to the central points of the surfaces of the elementary cells.

all magnetic field values and the values of the material parameter a are attached to the central points of the surfaces of the elementary cells. The average material parameters $\overline{a}(\mathbf{x})$ and $\overline{b}(\mathbf{x})$ in those points are obtained by averaging over a and b in the cells adjacent to the grid point under consideration. Discretizing the computational domain Ω in this way, and using grid versions of the integrals in (52), (53), we arrive after elimination of the magnetic field vectors at the following system

$$\mathbf{A}^T \mathbf{D}_{\bar{l}} \mathbf{D}_{\mu}^{-1} \mathbf{D}_{A}^{-1} \mathbf{A} \mathbf{D}_{l}\, e \;-\; k_0^2 \mathbf{D}_{\epsilon}\, e \;=\; -i\omega\mu_0 \mathbf{D}_{\bar{A}}\, j \;-\; \mathbf{A}^T \mathbf{D}_{\bar{l}} \mathbf{D}_{\mu}^{-1}\, m. \tag{54}$$

Here, e, j and m denote the (vectors of the discretized) electric field, the electric source currents, and the magnetic source currents, respectively. The symbols $\mathbf{D}_\epsilon$ and $\mathbf{D}_\mu$ denote diagonal matrices that contain the material parameters $\bar{\epsilon}$ and $\bar{\mu}$, and the symbols $\mathbf{D}_{\bar{l}}$, $\mathbf{D}_A$, $\mathbf{D}_l$, and $\mathbf{D}_{\bar{A}}$ denote diagonal matrices that contain information about the geometry of the grid. The matrix $\mathbf{A}$ models essentially the line integrals of (52) and (53). We mention that system (54) can be considered as a discretized version of the vector Helmholtz equation

$$\nabla \times (\bar{\mu}_r^{-1} \cdot \nabla \times \mathbf{E}) \;-\; k_0^2 \bar{\epsilon}_r \cdot \mathbf{E} \;=\; -i\omega\mu_0 \mathbf{J} \;-\; \nabla \times \bar{\mu}_r^{-1} \cdot \mathbf{M}, \tag{55}$$

which is commonly used in finite element codes.

After some further manipulation, the system (54) is solved iteratively, for example, by using the Bi-CGSTAB scheme of van der Vorst [44]. For more details we again refer to [17, 18, 22].

Acknowledgments

We thank N. J. Champagne (LLNL) for supplying us with the electromagnetics forward modeling code FDFD prior to publication. We thank H. M. Buettner (LLNL) for further assistance with the use of the EM code and for supplying us with the basic Lost Hills model we used in our synthetic examples. Work of OD was performed with partial support from the AFOSR, from the Environmental Management Science Program of DOE, and by the NSF grant DMS97-09320. The work of HBA and JGB was performed under the auspices of the U.S. Department of Energy by the Lawrence Livermore National Laboratory under contract No. W-7405-ENG-48 and supported specifically by the Environmental Management Science Program of the Office of Environmental Management and by the Applied Mathematical Sciences Program in the Mathematical, Information and Computational Sciences Division. Work of GCP was supported in part by grant F49620-98-1-0211 from AFOSR and by the NSF, DMS 96228554.

References

[1] Alumbaugh D L and Morrison H F 1995 Monitoring subsurface changes over time with cross-well electromagnetic tomography *Geophysical Prospecting* **43** 873–902

[2] Alumbaugh D L and Morrison H F 1995 Theoretical and practical considerations for crosswell electromagnetic tomography assuming cylindrical geometry *Geophysics* **60** 846–870

[3] Ammari H and Bao G 2001 Analysis of the scattering map of a linearized inverse medium problem for electromagnetic waves *Inverse Problems* **17** 219–234

[4] Arridge S R 1995 Photon-measurement density functions. Part I: Analytical forms *Applied Optics* **34** (34) 7395-7409

[5] Arridge S R and Schweiger M 1995 Photon-measurement density functions. Part II: Finite-element-method calculations *Applied Optics* **34** (31) 8026-8037

[6] Arridge S (1999) Optical Tomography in Medical Imaging *Inverse Problems* **15** R41-R93

[7] Ascher U M and Petzold L R (1998) *Computer Methods for Ordinary Differential Equations and Differential-Algebraic Equations* (SIAM: Philadelphia)

[8] Balanis C A 1997 Antenna theory: analysis and design (Wiley: New York) p 169

[9] Beilenhoff K, Heinrich W and Hartnagel H L (1992) Improved finite-difference formulation in frequency domain for three-dimensional scattering problems *IEEE Trans. Microwave Theory Tech.* **40** 540–546

[10] Berenger J P (1994) A perfectly matched layer for the absorption of electromagnetic waves *J. Computational Phys.* **114** 185–200

[11] Berryman J G (2000) Analysis of approximate inverses in tomography I. Resolution analysis of common inverses *Optimization in Engineering* **1** 87–115

[12] Berryman J G (2000) Analysis of approximate inverses in tomography II. Iterative inverses *Optimization in Engineering* **1** 437–473

[13] Borcea L, Berryman J G, and Papanicolaou G C 1996 High Contrast Impedance Tomography *Inverse Problems* **12** 935–958

[14] Borcea L, Berryman J G, and Papanicolaou G C 1999 Matching pursuit for imaging high contrast conductivity *Inverse Problems* **15** 811–849

[15] Buettner H M and Berryman J G 1999 An electromagnetic induction tomography field experiment at Lost Hills, CA, in the *Proceedings of SAGEEP*, Oakland, CA, March 14–18, 663–672

[16] Cao Y, Li S, Petzold L R, and Serban R 2001 Adjoint Sensitivity Analysis for Differential-Algebraic Equations: Part I, The Adjoint DAE System to appear in *SIAM J. Sci. Comput.*

[17] Champagne N J II, Berryman J G, Buettner H M, Grant J B and Sharpe R M (1999) A finite-difference frequency-domain code for electromagnetic induction tomography, in the *Proceedings of SAGEEP*, Oakland, CA, March 14–18, 931–940

[18] Champagne II N J, Berryman J G, and Buettner H M (2001) FDFD: A 3D finite-difference frequency-domain code for electromagnetic induction tomography *J. Comp. Phys.* **170** 830–848

[19] Dierkes T, Dorn O, Natterer F, Palamodov V and Sielschott H 2001 Fréchet derivatives for some bilinear inverse problems, to appear in *SIAM J. Appl. Math.*

[20] Dines K A and Lytle R J 1979 Computerized geophysical tomography *Proc. IEEE* **67** 1065-73

[21] Dorn O 1998 A transport-backtransport method for optical tomography 1998 *Inverse Problems* **14** 1107-1130

[22] Dorn O, Bertete-Aguirre H, Berryman J G and Papanicolaou G C 1999 A nonlinear inversion method for 3D-electromagnetic imaging using adjoint fields *Inverse Problems* **15** 1523-1558

[23] Dorn O 2000 Scattering and absorption transport sensitivity functions for optical tomography *Optics Express* **7** (13) 492–506

[24] Dorn O, Miller E L and Rappaport C M 2000 A shape reconstruction method for electromagnetic tomography using adjoint fields and level sets *Inverse Problems* **16** 1119-1156

[25] Farquharson C G and Oldenburg D W 1996 Approximate sensitivities for the electromagnetic inverse problem *Geophysical Journal International* **126** 235-252

[26] Habashy T M, Groom R W and Spies B R 1993 Beyond the Born and Rytov approximations: A nonlinear approach to electromagnetic scattering *J. Geophys. Res.* **98** 1759–1775

[27] Haber E, Ascher U and Oldenburg D 2000 On optimization techniques for solving nonlinear inverse problems *Inverse Problems* **16** 1263-1280

[28] Jenkins F A and White H E 1957 *Fundamentals of Optics* (McGraw-Hill: New York) p 300

[29] Kuzuoglu M and Mittra R 1996 Frequency dependence of the constitutive parameters of causal perfectly matched anisotropic absorbers *IEEE Microwave Guided Wave Lett.* **6** 447–449

[30] Maurer H, Boerner D E and Curtis A 2000 Design strategies for electromagnetic geophysical surveys *Inverse Problems* **16** 1097-1117

[31] McGillivray P R and Oldenburg D W 1990 Methods for calculating Frechet derivatives and sensitivities for the non-linear inverse problem: a comparative study *Geophysical Prospecting* **38** 499-524

[32] McGillivray P R, Oldenburg D W, Ellis R G, and Habashy T M 1994 Calculation of sensitivities for the frequency-domain electromagnetic problem *Geophysical Journal International* **116** 1-4

[33] Natterer F 1986 *The Mathematics of Computerized Tomography* (Stuttgart: Teubner)

[34] Natterer F and Wübbeling F 1995 A propagation-backpropagation method for ultrasound tomography *Inverse Problems* **11** 1225-1232

[35] Natterer F (1996) Numerical Solution of Bilinear Inverse Problems *Preprints* “Angewandte Mathematik und Informatik” 19/96-N Münster

[36] Natterer F and Wübbeling F *Mathematical Methods in Image Reconstruction*, Monographs on Mathematical Modeling and Computation 5, SIAM 2001.

[37] Newman G A and Alumbaugh D L 1997 Three-dimensional massively parallel electromagnetic inversion I. Inversion *Geophys. J. Int.* **128** 345–354

[38] Petzold L, Serban R, Li S, Raha S, and Cao Y 2001 Sensitivity Analysis and Design Optimization of Differential-Algebraic Equation Systems, to appear, *Proc. NATO Advanced Research Workshop on Computational Aspects of Nonlinear Structural Systems with Large Rigid Body Motion*

[39] Ramirez A, Daily W, LaBrecque D, Owen E and Chesnut D 1993 Monitoring an underground steam injection process using electrical resistance tomography *Water Resources Res.* **29** 73–87

[40] Rath V 1999 Inversion in anisotropen 2D-Strukturen, technical report, Free University Berlin

[41] Sacks Z S, Kingsland D M , Lee R and Lee J F 1995 A perfectly matched anisotropic absorber for use as an absorbing boundary condition *IEEE Trans. Antennas Prop.* **43** 1460–1463

[42] Schwalenberg K and Rath V 1999 Magnetotellurische Sensitivitäten im 2D-Fall, technical report, Free University Berlin

[43] Spies B P and Habashy T M 1995 Sensitivity analysis of crosswell electromagnetics *Geophysics* **60** 834–845

[44] van der Vorst H A 1992 Bi-CGSTAB: A fast and smoothly converging variant of Bi-CG for the solution of non-symmetric linear systems *SIAM J. Sci. Stat. Comput.* **12** 631–644

[45] Vasco D W, Datta-Gupta A and Long J C S 1997 Resolution and uncertainty in hydrologic characterization *Water Resources Res.* **33** 379–397

[46] Ward S H and Hohmann G W 1987 Electromagnetic theory for geophysical applications, in *Electromagnetic Methods in Applied Geophysics – Theory*, Vol. 1, M. N. Nabighian (ed.), SEG, Tulsa, Oklahoma, 1987, pp 131–311

[47] Weidelt P 1995 Three-dimensional conductivity models: implications of electrical anisotropy. In Oristaglio M and Spies B (ed) *International Sumposium on Three-dimensional Electromagnetics, Oct 4-6, 1995, at Schlumberger-Doll Research, Ridgefield/Connecticut, USA,* pp 1-11

[48] Wilt M J, Schenkel C, Wratcher M, Lambert I, Torres-Verdin C and Tseng H W 1996 Crosshole EM for oil field characterization and EOR monitoring: Field examples from Lost Hills, California, LLNL UCRL-ID-123893, July 16, 1996